HHS Public Access

Author manuscript

Cell Rep. Author manuscript; available in PMC 2020 January 24.

Published in final edited form as:

Cell Rep. 2020 January 07; 30(1): 269–283.e6. doi:10.1016/j.celrep.2019.12.025.

TACC3 Regulates Microtubule Plus-End Dynamics and Cargo Transport in Interphase Cells

Colleen Furey[1], **Vladimir Jovasevic**[1], **Derek Walsh**[1,2,*]

[1]Department of Microbiology-Immunology, Feinberg School of Medicine, Northwestern University, Chicago, IL, USA

[2]Lead Contact

SUMMARY

End-binding proteins (EBs) are widely viewed as master regulators of microtubule dynamics and function. Here, we show that while EB1 mediates the dynamic microtubule capture of herpes simplex virus type 1 (HSV-1) in fibroblasts, in neuronal cells, infection occurs independently of EBs through stable microtubules. Prompted by this, we find that transforming acid coiled-coil protein 3 (TACC3), widely studied in mitotic spindle formation, regulates the cytoplasmic localization of the microtubule polymerizing factor chTOG and influences microtubule plus-end dynamics during interphase to control infection in distinct cell types. Furthermore, perturbing TACC3 function in neuronal cells resulted in the formation of disorganized stable, detyrosinated microtubule networks and changes in cellular morphology, as well as impaired trafficking of both HSV-1 and transferrin. These trafficking defects in TACC3-depleted cells were reversed by the depletion of kinesin-1 heavy chains. As such, TACC3 is a critical regulator of interphase microtubule dynamics and stability that influences kinesin-1-based cargo trafficking.

In Brief

While EB proteins are widely studied as master regulators of microtubule plus-end dynamics, Furey et al. report EB-independent regulation of microtubule arrays and cargo trafficking by the transforming acid coiled-coil-containing protein, TACC3. By controlling the formation of detyrosinated stable microtubule networks, TACC3 influences kinesin-1-based sorting of both host and pathogenic cargoes.

Graphical Abstract

*Correspondence: derek.walsh@northwestern.edu.

AUTHOR CONTRIBUTIONS

C.F. performed most of the experiments described; C.F. and V.J. performed the knockdown experiments and analyzed the data. C.F., V.J., and D.W. designed the experiments and interpreted the results. C.F. drafted, D.W. edited, and all of the authors finalized the manuscript.

DECLARATION OF INTERESTS

The authors declare no competing interests.

SUPPLEMENTAL INFORMATION

Supplemental Information can be found online at https://doi.org/10.1016/j.celrep.2019.12.025.

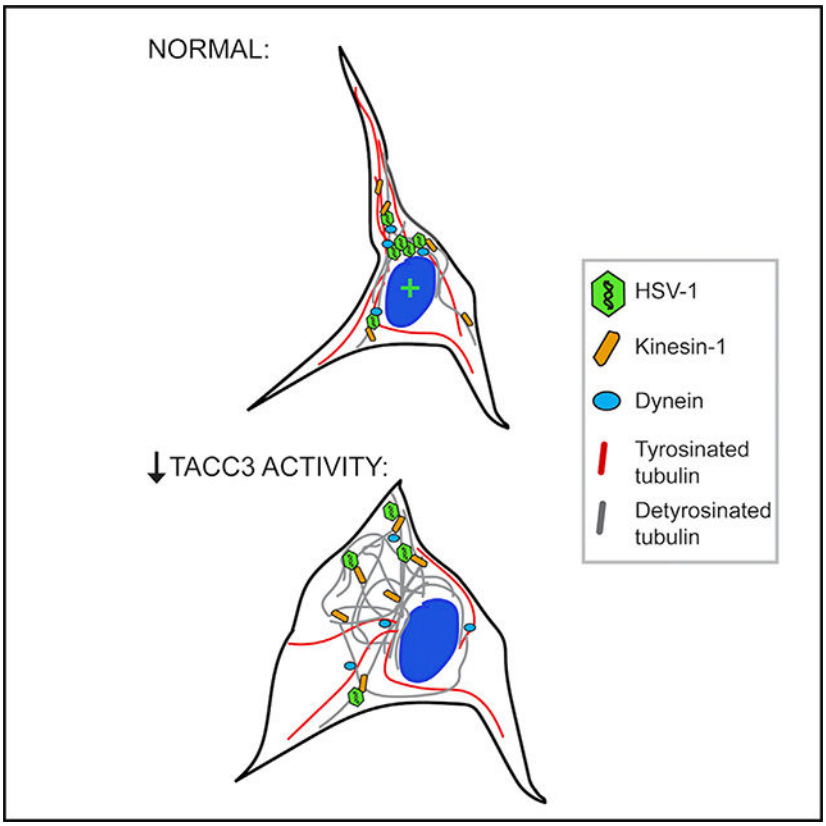

INTRODUCTION

The microtubule (MT) network regulates processes ranging from cell division and motility to cargo transport (Akhmanova and Steinmetz, 2008, 2015; Stephens, 2012). Filaments nucleate from an MT organizing center (MTOC) and explore the cytosol through phases of polymerization, pause, and catastrophe as tubulin heterodimer subunits are either added or removed from their more dynamic plus-end (Jánosi et al., 2002; Kristofferson et al., 1986). The MT plus-end transiently contains guanosine triphosphate (GTP)-bound tubulin before it is hydrolyzed to guanosine diphosphate (GDP)-tubulin within the filament lattice (Guesdon et al., 2016; Howard and Hyman, 2003; Jánosi et al., 2002). This GTP-tubulin cap enables the growing MT plus-end to be recognized by members of the end-binding (EB) family of proteins, EB1–EB3 (Guesdon et al., 2016; Komarova et al., 2009; Maurer et al., 2012). At the plus-end, EBs can directly suppress catastrophe events, leading to enhanced MT growth (Komarova et al., 2009). EBs also bind and recruit other plus-end tracking proteins (+TIPs) to form functional nodes that control filament growth, stability, spatial organization, and interactions with targets such as cortical actin or cellular cargoes (Akhmanova and Steinmetz, 2015; Honnappa et al., 2009; Komarova et al., 2005; Lansbergen et al., 2006; Zhang et al., 2015). While several +TIPs have been identified in recent years, many of which can bind MT filaments independently, most require EB proteins to mediate their specific accumulation at MT plus-ends. For this reason, EBs are widely considered to be master regulators of MT function (Akhmanova and Steinmetz, 2015).

Other proteins do operate at the MT plus-end independently of EB proteins, yet their functions are less well defined. chTOG (colonic and hepatic tumor-overexpressed gene) is a microtubule polymerase that binds soluble tubulin dimers and catalyzes their addition to MT plus-ends (Brouhard et al., 2008; Gard and Kirschner, 1987;Slep and Vale, 2007). chTOG binds MT plus-ends autonomously, but its optimal plus-end localization depends upon recruitment by transforming acidic coiled-coil-containing (TACC) proteins (Hussmann et al., 2016; Mortuza et al., 2014). Homologs of both chTOG and TACCs are widely conserved across eukaryotes (Gard et al., 2004; Still et al., 2004). Humans express three TACC proteins (TACC1–TACC3) and along with chTOG, TACCs have been extensively studied in the context of mitotic spindle organization during cell division and in cancer (Ding et al., 2017; Gard et al., 2004; Mortuza et al., 2014; Peset and Vernos, 2008; Raff, 2002; Still et al., 1999, 2004; Thakur et al., 2014), although TACC3 is the most widely studied and best-characterized family member. By recruiting chTOG, TACC3 functions at the centrosome to regulate MT nucleation, along the MT lattice to stabilize the spindle apparatus, and at the MT plus-end to promote mitotic spindle elongation (Gergely et al., 2000, 2003; Kinoshita et al., 2005; Lee et al., 2001; Lin et al., 2010; Mortuza et al., 2014). However, our understanding of the potential functions of TACC3 in interphase remains limited (Chanez et al., 2015; Gunzelmann et al., 2018; Kume et al., 2018; Nakamura et al., 2012; Nakaseko et al., 2001; Trogden and Rogers, 2015). In yeast, the homolog of TACC3, Alp7, recruits Alp14/TOG to the nucleus during cell division or to the cytoplasm during interphase. The absence of Alp7 results in short spindles during mitosis or defects in MT growth and organization in interphase (Hussmann et al., 2016; Ling et al., 2009; Sato et al., 2004, 2009; Sato and Toda, 2007; Zheng et al., 2006). Moreover, yeast Alp7 mediates the recruitment of Alp14/TOG to MT plus-ends *in vitro* (Hussmann et al., 2016). Evidence for similar interphase functions of TACC3 is also emerging in higher organisms. TACC3 has been shown to recognize interphase MT plus-ends in *Drosophila* and *Xenopus* embryonic cells, as well as in human HeLa and RpeI cells (Gutiérrez-Caballero et al., 2015; Lee et al., 2001; Nwagbara et al., 2014). However, while TACC3 homologs promote interphase MT dynamics in both *Drosophila* and *Xenopus* systems, modulating TACC3 levels has been reported to have no effect in HeLa cells (Erdogan et al., 2017; Gutiérrez-Caballero et al., 2015; Long et al., 2013; Nwagbaraetal., 2014).Thus, the potential role of TACC3 in regulating MT dynamics and its broader functionality during interphase remains poorly understood, particularly in human cells.

As intracellular pathogens, viruses are dependent upon MTs to facilitate their replication (Naghavi and Walsh, 2017). However, the importance of +TIPs during infection has only recently begun to emerge (Delaney et al., 2017; Jovasevic et al., 2015; Naghavi et al., 2013; Procter et al., 2018; Sabo et al., 2013). Of particular relevance to this study, we previously showed that EB1 and the +TIP, cytoplasmic linker-associated protein 170 (CLIP170), are required for herpes simplex virus type 1 (HSV-1) particles to load onto dynamic MTs for subsequent motor-mediated transport to the nucleus in dermal fibroblasts (Jovasevic et al., 2015). However, *in vivo* HSV-1 infects a variety of cell types, which include epithelial, dermal, and neuronal cells (Roizman et al., 2013). Many cell types contain mixtures of both dynamic and stable MT arrays, but neuronal cells contain a particularly high proportion of stabilized filaments (Baas and Black, 1990; Brady, 1993; Sahenk and Brady, 1987; Song et

al., 2013). While dynamic MTs have a relatively short half-life, stable MTs are long-lived and therefore accumulate higher levels of several tubulin post-translational modifications (PTMs) (Janke and Bulinski, 2011). Tubulin PTMs include acetylation at lysine 40, which resides within the lumen of the filament and confers mechanical strength against breakage (Portran et al., 2017; Xu et al., 2017). While acetylation can occur quite rapidly, another PTM, tubulin detyrosination, appears to occur more gradually and accumulates largely on stable MTs. Tubulin detyrosination occurs on the cytosolic side of the MT filament (Hallak et al., 1977; Rodrĭguez et al., 1973) and alters interactions with motors to favor kinesin-1 activity (Cai et al., 2009; Dunn et al., 2008; Liao and Gundersen, 1998). As such, distinct properties conferred by different tubulin PTMs enable stable MTs to serve as long-lived, specialized tracks for cargo sorting (Janke and Bulinski, 2011).

Here, in examining the role of +TIPs during HSV-1 infection of different human cell types, we unexpectedly reveal that EB1 and CLIP170 are required for the infection of fibroblasts but not neuronal cells. In neuronal cells, infection was largely mediated by stable, detyrosinated MT networks that formed independently of EB1. Stemming from this, we find that TACC3 regulates interphase MT dynamics and in neuronal cells, by regulating the organization of detyrosinated MT arrays, influences kinesin-1-based sorting of both pathogenic and cellular cargoes.

RESULTS

Stable Microtubules Mediate EB-Independent HSV-1 Infection in Neuronal Cells

EB1 and CLIP170 are required for HSV-1 infection in normal human dermal fibroblasts (NHDFs) (Jovasevic et al., 2015). This prompted us to test whether these +TIPs also functioned during the infection of neuronal cells. To do this, we compared the effects of EB1 or CLIP170 depletion on infection in NHDFs versus SK-N-SH cells, a human neuroblastoma cell line used to model neuronal infection (Biedler et al., 1973; Gordon et al., 2013) (Figures S1A and S1B). Western blot (WB) analysis revealed that while knockdown of either EB1 or CLIP170 suppressed early infection in NHDFs, as detected by the reduced abundance of the viral immediate early infected cell protein 4 (ICP4), depletion of either factor had no effect on infection in SK-N-SHs (Figure 1A). While EB1 is the dominant EB family member in many cell types (Akhmanova and Steinmetz, 2015; Komarova et al., 2009), depletion of the closely related family member EB3, either alone or in combination with EB1, or depletion of the more distantly related EB2, had no detectable effect on the expression of early viral proteins in SK-N-SHs (Figures 1B and 1C). Furthermore, bafilomycin-A1 (BafA) blocked the infection of SK-N-SHs by vesicular stomatitis virus (VSV) but not HSV-1 (Figure 1D), demonstrating that HSV-1 did not use alternative low-pH fusion (e.g., endocytosis) over its natural route of membrane fusion to enter these cells. This suggested that EB1-mediated dynamic microtubule capture was not a significant mechanism for the infection of SK-N-SHs.

We next used WB and immunofluorescence (IF) analysis to compare the nature of MT networks in both cell types. Samples were probed with antibodies against total or tyrosinated α-tubulin, as well as detyrosinated- or acetylated-α-tubulin. Results showed that NHDFs contained both tyrosinated and acetylated MTs, but little to no discernible detyrosinated

tubulin or filaments (Figures 1E and 1F). By contrast, SK-N-SHs contained a high proportion of acetylated and detyrosinated MTs, which extended from a perinuclear region (Figures 1E and 1F).

To determine whether these differences in tubulin PTMs reflect differences in MT stability that influence infection, we treated NHDFs and SK-N-SHs with DMSO solvent control or different doses of the MT depolymerizing agent nocodazole before infection with HSV-1. Low nanomolar concentrations of nocodazole either depolymerize or dampen the growth of dynamic MTs, but they do not affect stable filaments; by contrast, higher micromolar concentrations result in the loss of both dynamic and stable MTs (Kreis, 1987; Liao et al., 1995). In NHDFs that contain a high proportion of dynamic MTs, several tyrosinated MT filaments persisted in cultures treated with 500 nM nocodazole (Figure S1C). However, EB1 no longer formed comet-like staining patterns, demonstrating that despite the persistence of some filaments, MT dynamics were dampened under these conditions (Figure S1D). In SK-N-SHs that contain a mix of tyrosinated and detyrosinated filaments, 500 nM nocodazole depolymerized tyrosinated MTs and caused a loss of EB1 comet staining, but detyrosinated MTs persisted (Figures S1C–S1F). The accumulation of detyrosinated tubulin combined with resistance to nanomolar concentrations of nocodazole is a defining characteristic of stable MTs. Finally, treating cells with 10 μM nocodazole depolymerized dynamic and stable MTs in both cell types (Figures S1C and S1E).

To test the effects on virus translocation to the nucleus, we stained samples for the capsid protein, VP5. Staining and quantification showed that while virus particles reached the nuclear periphery in both cell types in DMSO-treated controls, this was impaired in NHDFs treated with 500 nM nocodazole (Figures 1G and S1C). By contrast, in SK-N-SHs, HSV-1 particles accumulated along perinuclear detyrosinated MT networks in both DMSO-treated and 500 nM nocodazole-treated samples (Figures 1G and S1C). However, 10 μM nocodazole depolymerized both dynamic and stable MTs and impaired the nuclear accumulation of HSV-1 in both NHDFs and SK-N-SHs (Figures 1G and S1C). WB analysis confirmed these IF-based observations, showing that expression of the HSV-1 immediate early proteins ICP0 and ICP4 was potently blocked by either high- or low-dose nocodazole in NHDFs, while in SK-N-SHs, viral gene expression was relatively resistant to low-dose nocodazole treatment (Figure 1H). This supported the notion that dynamic MTs mediate infection in NHDFs, while stable MTs mediate infection in SK-N-SHs.

We next tested whether these effects on HSV-1 infection reflected defects in virus entry by staining nocodazole-treated, HSV-1-infected cells for the viral glycoprotein gB together with VP5. In this assay, VP5 capsids that do not co-stain for gB represent viral particles that have lost their envelope after fusing into the cytosol, while those that co-stain for both proteins represent unfused particles. Results showed that nocodazole did not block HSV-1 fusion in either cell type, while infections at 4°C validated the ability of this assay to detect impairments in virus fusion (Figures S2A–S2D). Despite differences in actin organization between the two cell types, no gross changes in actin staining were detected in nocodazole-treated SK-N-SHs or NHDFs compared with DMSO controls (Figure S2E). As such, while we cannot rule out subtle effects on actin organization or dynamics that may influence infection, there were no striking differences in how nocodazole affected actin organization

that may explain the differential sensitivity of infection to this drug between these two cell types. Cumulatively, nocodazole exerted a post-entry effect on viral translocation to the nucleus that correlated with the effects on dynamic MTs in NHDFs or stable MTs in SK-N-SHs. This was also in line with the relative sensitivity of infection to the depletion of EB1 in each cell type (shown earlier), further suggesting that EB1 may not play a major role in regulating stable MTs in SK-N-SHs.

TACC3 Regulates Stable MT Networks in SK-N-SHs

To test this, we determined the effects of EB1 depletion on MT networks in SK-N-SHs. While EB1 regulates several aspects of MT plus-end dynamics, potent depletion of EB1 had little effect on the levels or organization of acetylated or detyrosinated MTs in SK-N-SHs (Figures 2A, 2B, and S2F). This prompted us to explore the potential contributions from TACC3, based on recent reports that TACC3 can track MT plus-ends independently of EB1 in interphase cells (Gutiérrez-Caballero et al., 2015; Nwagbara et al., 2014). To do so, we examined the expression of TACC protein family members and chTOG. WB analysis showed that both cell types express similar levels of chTOG but that SKN-SHs express higher levels of TACC proteins, in particular TACC3 (Figure S3A). Higher levels of TACC3 in SK-N-SHs were confirmed by measuring relative fluorescence intensity in IF images (Figures S3B and S3C). Notably, NHDFs and SK-NSHs contain a significantly smaller fraction of cells undergoing mitosis at any given time than more widely used cell lines (Figures S3D and S3E). In addition, while TACC3 accumulated along the mitotic spindle in this small fraction of cells (Figure S3D), TACC3 was diffusely cytoplasmic in the larger interphase population of both cell types (Figure S3C). As such, both cell types are relevant to the study of the functionality of TACC3 in interphase cells and in infection.

To test whether TACC3 regulated MT networks, we treated SK-N-SHs with either of two independent small interfering RNAs (siRNAs), which resulted in different degrees of TACC3 depletion (Figure 2C). The use of the most potent siRNA (TACC3-I) resulted in the accumulation of high levels of acetylated and detyrosinated MTs, which appeared disorganized (Figures 2A, 2B, and 2D). The potent depletion of TACC3 also resulted in changes in cell diameter compared with control siRNA-treated SK-N-SHs, which were not observed in EB1-depleted cells (Figures 2A, 2B, S3F, and S3G). The use of the second, less potent siRNA (siTACC3-II) resulted in intermediate phenotypes (Figures 2A, 2B, 2D, S3F, S3G), establishing a dose-dependent effect of TACC3 loss on the organization of stable MTs and cell diameter. To confirm that these were not off-target effects, we rescued TACC3 expression in TACC3-I siRNA-treated SK-N-SHs (Figure 2E). Due to species incompatibility between TACC3 and detyrosinated tubulin antibodies, we stained for acetylated tubulin, as both modifications arise on stable MTs (Figure 2A). IF imaging and quantification showed that restoring TACC3 expression reversed the effects of TACC3 depletion on acetylated MTs and cell diameter (Figures 2F–2H). Finally, we used the Golgi as an additional readout for the effects of TACC3, as the Golgi is dependent on MTs to maintain its organization (Chabin-Brion et al., 2001; Procter et al., 2018). IF imaging and measurements of the area stained by the *trans*-Golgi marker TGN46 revealed that TACC3 depletion resulted in a significant increase in TGN area (Figures 2I and 2J). Changes in cell diameter and TGN area were not observed in cells depleted of EB1 (Figures S3G and S3H),

and these phenotypes were reversed by restoring TACC3 expression in TACC3-I siRNA-treated cells (Figures 2I and 2J). Phenotypes were only partially rescued, as we transiently reintroduced TACC3 expression for just the final day of siRNA treatment.

TACC3 Regulates chTOG Localization and MT Plus-End Growth in Interphase Cells

We next explored how TACC3 could exert these effects on MT organization and whether it exhibited cell-specific differences in functionality between SK-N-SHs or NHDFs. Given its established functions at centrosomes and spindle poles during mitosis, we examined whether TACC3 exerted effects on centrosomes or MT nucleation in interphase cells.

NHDFs or SK-N-SHs were transfected with control or TACC3-I siRNA. Staining for both pericentrin and γ-tubulin, together with measurements of pericentrin fluorescence intensity, showed that TACC3 loss did not grossly affect centrosomes in either cell type, although subtle changes cannot be ruled out (Figure S4A). Moreover, tyrosinated tubulin staining suggested that overall MT organization and cell shape were largely unaffected in NHDFs, while SK-N-SHs again exhibited changes in MT organization and morphology upon TACC3 depletion. This provided the first evidence of potential cell-specific differences in TACC3 function.

To test the effects on MT nucleation, we examined the repolymerization of MTs in nocodazole washout assays. siRNA-treated cells were incubated with 10 μM nocodazole to depolymerize MTs, followed by washout and staining for α-tubulin. In NHDFs, TACC3 depletion had no significant effect on tubulin levels at centrosomes or the average area of new MTs extending from centrosomes compared with controls (Figures S4B and S4C). Similar results were observed in SK-N-SHs, although high levels of α-tubulin throughout the cytosol made it challenging to accurately quantify the area of new MTs (Figure S4D). However, these MTs were also acetylated, and quantifying their area showed that, like NHDFs, TACC3 depletion had no significant effect on the formation of new MTs in SK-N-SHs (Figures S4E and S4F).

As TACC3 did not significantly affect MT nucleation, we next tested whether it affected MT plus-end dynamics. As a central plus-end recognition factor, EB1 proteins form a comet-like staining pattern as they track growing MT tips (Akhmanova and Steinmetz, 2015). In SK-N-SHs, TACC3-I and TACC3-II siRNAs revealed a dose-dependent effect of TACC3 depletion on the number of EB1 comets per cell, which also correlated with an increase in detyrosinated MTs (Figures 3A and 3B). Fluorescence intensity comparisons further highlighted the correlation between the degree of TACC3 loss and reductions in EB1 staining across individual cells (Figure S5A). Similar effects of TACC3 depletion on EB1 staining were observed in NHDFs (Figures S5B–S5D), suggesting that TACC3 regulates MT dynamics in both cell types. We further confirmed changes in MT dynamics by performing time-lapse fluorescence microscopy using NDHFs that stably express GFP-CLIP170 (Procter et al., 2018). CLIP170 tracks grow MT plus-ends in a manner that is both EB1 dependent and independent (Dixit et al., 2009), making it ideal to study broader MT behavior. In control siRNA-treated NHDFs, GFP-CLIP170 exhibited typical plus-end tracking behaviors (Figure S5E; Video S1). However, TACC3 depletion caused notable changes in CLIP170 behavior. In some instances, GFP-CLIP170 extended down the lattice

of MTs that did not appear to grow or shrink. Beyond these, the number of GFP-CLIP170 comets was reduced, and the comets that formed were slower and more elongated. This demonstrated that TACC3 influenced MT plus-end growth as suggested by EB1 staining.

To validate siRNA-based findings, we used a dominant-negative approach. GFP- or FLAG-tagged TACC3 forms aggregates that recruit the MT polymerase chTOG (Gergely et al., 2000; Lee et al., 2001). Based on this, we postulated that tagging may generate a dominant-negative TACC3 that sequesters chTOG. In line with this, the expression of untagged TACC3 did not result in the formation of aggregates, while the expression of FLAG-tagged TACC3 formed aggregates in both SK-NSHs and NHDFs (Figures 3C–3E, S5F, and S5G). In SK-N-SHs, FLAG-TACC3 expression resulted in the elongation of EB1 comets (Figure 3F). However, these effects proved difficult to quantify, as this dominant-negative approach was less effective in SK-N-SHs, likely due to their high basal levels of TACC3 expression. More robust and readily quantifiable effects were observed in NHDFs that express lower levels of endogenous TACC3. Compared with controls, FLAG-TACC3 expression resulted in both a decrease in the number of EB1 comets per cell and an increase in the length of EB1 comets, which is indicative of a reduction in the number and growth rate of dynamic MTs, respectively (Figures S5H–S5J). FLAG-TACC3 expression also caused an increase in acetylated MTs in NHDFs (Figure S5K), suggesting an increase in PTMs accumulating on less dynamic MTs. Cumulatively, these data demonstrated that TACC3 regulated MT plus-end dynamics in both cell types.

We next confirmed that our FLAG-TACC3 dominant-negative approach did indeed sequester chTOG. To accommodate costaining, a mouse anti-FLAG antibody that generates more background signal had to be used. Despite this, aggregates of FLAG-TACC3 were readily discernible in both cell types, and chTOG was sequestered within these aggregates (Figures 3G and S6A) (Gergely et al., 2000). Testing the effects of TACC3 depletion, WB analysis showed that the total abundance of chTOG was unaffected in either SK-N-SHs or NHDFs (Figures 3H and S6B). However, IF imaging and quantification showed that chTOG accumulated in the nucleus in TACC3-depleted cells (Figures 3I, 3J, S6C, and S6D), similar to the reported effects of Alp7 deletion in yeast (Ling et al., 2009; Sato and Toda, 2007). While these cells are relatively flat and well suited to single-plane widefield imaging, we confirmed the nuclear accumulation of chTOG in TACC3-depleted cells using confocal microscopy and maximum projection z stacks (Figures 3K, 3L, S6E, and S6F; Video S2). These approaches revealed that TACC3 regulates the cytoplasmic localization of chTOG, with the loss of TACC3 resulting in its nuclear localization, while dominant-negative TACC3 sequestered chTOG in the cytoplasm.

TACC3 Regulates Infection and Kinesin-1-Based Trafficking in SK-N-SHs

Our data to this point showed that TACC3 perturbations resulted in similar defects in MT plus-end growth and induced acetylated MTs in both SK-N-SHs and NHDFs. Acetylation occurs rapidly and is not exclusive to stable MTs. By contrast, dysregulation of stable detyrosinated MT networks and changes in cell morphology only occurred in SK-N-SHs. This suggested that while TACC3 broadly regulates MT dynamics, it has cell-specific functions that control stable MTs in SK-N-SHs and may influence HSV-1 infection.

To test this, we treated NHDFs or SK-N-SHs with control or TACC3 siRNAs and then infected them with HSV-1. IF imaging and quantification showed that TACC3 depletion caused a significant decrease in the number of nuclei expressing the viral protein ICP4 and in the accumulation of $VP5^+$ viral particles around the nuclei of either NHDFs or SK-N-SHs (Figures 4A, 4B, and S6G, and S6H). While its effects on MT dynamics would make it predictable that TACC3 depletion would affect infection in NHDFs, infection was also impaired in TACC3-depleted SK-NSHs. Notably, using the same assays, EB1 depletion did not affect either ICP4 expression or virus accumulation around the nucleus in SK-N-SHs (Figures 4C and 4D).

Next, we tested whether effects on HSV-1 infection in SK-NSHs reflected defects in virus entry or trafficking. We stained siRNA-treated cells infected with HSV-1 for the viral glycoprotein gB together with the capsid protein VP5 (Figures 4E and 4F). As described earlier, VP5 capsids that do not co-stain for gB represent fused particles. Compared with controls, TACC3 depletion caused an initial reduction in the number of fused particles in the cytosol at 30 min post-infection, but a sizeable number of fused particles were detectable by 60 min (Figures 4E and 4F). This suggested that TACC3 depletion slowed but did not block HSV-1 entry. To test whether TACC3 also affected the trafficking of HSV-1 particles that eventually enter the cytosol, we infected siRNA-treated SK-N-SHs with HSV-1 carrying a GFP-tagged virion protein, VP26 (Desai and Person, 1998). Live-cell video microscopy showed that in control siRNA-treated cells, early in the entry process (30 min), virus particles were distributed throughout the cell and exhibited bidirectional short- and long-range movements. By 60 min, many particles had reached the nucleus, where they dock and become static (Figure 4G; Video S3). Particle tracking further showed that viruses that were still motile exhibited net retrograde movement toward the nucleus (Figures 4H and 4I). By contrast, in TACC3-depleted cells, many virus particles remained at the cell periphery at both 30- and 60-min time points, in line with the slower entry detected using fixed imaging approaches. Moreover, particle tracking showed that motile viruses exhibited net anterograde movement away from the nucleus (Figures 4H and 4I), suggesting increased kinesin-based movement in TACC3-depleted cells. In addition, virus particles near the nucleus appeared to be distributed throughout the enlarged detyrosinated MT network formed in TACC3-depleted cells.

Tubulin detyrosination reduces dynein and increases kinesin-1 affinity and motor processivity on MTs (Cai et al., 2009; Dunn et al., 2008; Liao and Gundersen, 1998; McKenney et al., 2016). As such, the changes in abundance and organization of detyrosinated MTs in TACC3-depleted SK-N-SHs may favor kinesin-1 activity and impair the inward transport of virus particles. If this were the case, then suppressing kinesin-1 activity should rescue infection in TACC3-depleted cells. To test this, we treated ssSK-N-SHs with TACC3-I siRNAs, either alone or in combination with siRNAs targeting the kinesin-1 heavy-chain isoform Kif5B (Figure 5A). IF analysis of siRNA-treated cells suggested that TACC3 depletion did not cause gross defects in Kif5B localization, although more subtle effects cannot be ruled out (Figure 5B). Cultures were then infected with HSV-1 and fixed at 4 h post-infection (hpi), followed by co-staining with VP5 and gB. IF analysis and quantification showed that in control cells, fused viral particles accumulated at specific regions of the nuclear periphery (Figures 5C and 5D). This pattern of accumulation was

reduced in TACC3-depleted cells, but this defect was rescued by Kif5B depletion. We also examined effects on virus movement. siRNA-treated cells were infected with HSV-1 GFP-VP26 virus for 60 min to allow the fusion of a significant fraction of virus under all conditions, followed by live-cell video microscopy. Time-lapse imaging and particle tracking revealed that in control siRNA-treated cells, virus particles exhibited net retrograde movements and accumulated around the nuclear periphery (Figures 5E–5G; Video S4). While TACC3 depletion again impaired virus movement and translocation to the nucleus, these defects were rescued in TACC3-I siRNA-treated cells by depleting Kif5B (Figures 5E–5G; Video S4).

These findings suggested that TACC3 regulates the organization of detyrosinated MT networks that control kinesin-1-based trafficking pathways exploited by HSV-1, but that may also affect the trafficking of cellular cargoes. To test this, we examined transferrin uptake and localization. Following endocytosis, transferrin-containing endosomes enter the recycling endosomal pathway, whereby endosomes undergo either fast recycling to the plasma membrane or slow recycling to the perinuclear endocytic recycling compartment (Xie et al., 2016). Furthermore, transferrin is known to be recycled from perinuclear regions to the cell periphery on detyrosinated MTs by kinesin-1 (Lin et al., 2002).

We examined the sensitivity of Alexa Fluor 647-transferrin uptake and sorting to the perinuclear space in nocodazole-treated SK-N-SHs. While overall, Alexa Fluor 647-transferrin intensity was partially decreased at 500 nM nocodazole, suggesting that dynamic MTs maximize the degree of transferrin uptake, it continued to accumulate at the perinuclear space (Figures 6A and 6B). By contrast, at 10 μM nocodazole, both transferrin uptake and sorting to the nuclear periphery were impaired. It is important to note that although images show a very strong reduction in the intensity of transferrin accumulation at this perinuclear region in cells treated with 10 μM nocodazole, the presence of randomly localized and diffuse transferrin-positive vesicles underestimates this effect in quantification approaches.

To examine the effects of TACC3 depletion and the role of kinesin-1, we added Alexa Fluor 647-transferrin to siRNA-treated SK-N-SHs, followed by time-lapse fluorescence microscopy. While Kif5B is the dominant isoform in many cell types, and its depletion rescued HSV-1 infection, we depleted TACC3 alone or in combination with either Kif5B or all three Kif isoforms (A, B, and C) (Figure 6C). Time-lapse imaging showed that in control cells, transferrin trafficked along cellular projections into and out of the broader cytoplasmic space, and it concentrated in specific perinuclear regions (Figure 6D; Video S5). This would be expected for both fast recycling and entry into late endosomal pathways. In TACC3-depleted cells, transferrin uptake appeared reduced, and transferrin that was taken into cells did not concentrate at perinuclear regions. However, co-depletion of either Kif5B alone or Kif5A–Kif5C largely restored the uptake and accumulation of transferrin at perinuclear regions. This demonstrated that similar to HSV-1, the depletion of Kif5B alone was sufficient to rescue defects in transferrin trafficking caused by the loss of TACC3. We confirmed these observations by staining fixed cells for detyrosinated tubulin, directly imaging and quantifying the accumulation of Alexa Fluor 647-transferrin at perinuclear sites (Figures 6E and 6F). This further demonstrated how transferrin penetrated deeper into the

enlarged detyrosinated MT networks to reach the perinuclear space in TACC3-depleted cells when Kif5B was co-depleted (Figures 6E and 6F).

Notably, the perinuclear accumulations of transferrin in TACC3 and Kif5B co-depleted cells were more enlarged than those in control cells. Staining of fixed cells showed that depletion of Kif5B did not reverse the effects of TACC3 depletion on detyrosinated MTs or the enlargement of cells (Figure 6E). Moreover, Kif5B depletion did not rescue the effects of TACC3 depletion on Golgi size (Figures 6G and 6H). This suggested that kinesin-1 did not influence cell shape or Golgi organization that is largely controlled by MTs directly, but it played an important role in how cellular and pathogenic cargoes reach the perinuclear space in the presence of detyrosinated MT networks that are controlled by TACC3.

DISCUSSION

The importance of EB proteins in regulating MT dynamics is well characterized across many cell systems (Akhmanova and Steinmetz, 2015). In line with our own previous studies (Jovasevic et al., 2015), EB1 and CLIP170 play critical roles in mediating early HSV-1 infection in human fibroblasts, wherein virus transport is mediated by dynamic MT capture. However, neither CLIP170 nor EB1, along with other EB family members, were required for HSV-1 infection in SK-N-SHs. This led us to discover that EB proteins do not detectably affect the formation of detyrosinated MT networks and HSV-1 translocation to the nucleus in these cells. It is important to note that these observations do not rule out more subtle roles for EB proteins. However, they reveal how the importance of EB proteins differs across cell types and processes, in which other MT regulators can play more dominant roles. EB1 and EB3 play distinct and very specialized roles during mitosis and cytomegalovirus infection (Ban et al., 2009; Ferreira et al., 2013; Procter et al., 2018). Despite our extensive knowledge of EB proteins, much remains to be learned about the contributions of other factors that control MT plus-end dynamics.

Despite recent evidence that TACC3 exhibits autonomous +TIP activity, our understanding of how and when it functions outside mitosis is limited. In *Xenopus* embryos, XTACC3 regulates the recruitment of XMAP215 (chTOG) to MT plus-ends to control filament dynamics and axon elongation (Nwagbara et al., 2014). Similar functions are suggested in yeast, in which Alp7 (TACC3) also regulates the cytoplasmic and nuclear localization of Alp14 (TOG) (Ling et al., 2009; Sato and Toda, 2007). Our findings show that TACC3 similarly controls chTOG localization and promotes MT plus-end growth in human fibroblasts and neuronal cells. Perturbing TACC3 activity did not affect the initial regrowth of MTs, yet it significantly reduced the levels of EB1 comets and altered CLIP170 tracking behavior. This is reminiscent of its functions in mitotic spindle formation and suggests that TACC3 predominantly acts to promote MT polymerization in the cytosol after nucleation, where growing MT ends are then tracked by other +TIPs such as EB1. Once at MT plus-ends, however, the functional importance of EB1 varies with cell type and context.

Although TACC3 regulates MT dynamics in both cell types tested, we find that it also has cell-specific functions. Unlike NHDFs that harbor a high proportion of dynamic MTs, perturbing TACC3 functionality in SH-N-SHs resulted in the formation of extensive stable,

detyrosinated networks, accompanied by changes in cell morphology. Kif5B co-depletion did not reverse the effects of TACC3 knockdown on detyrosinated MTs, nor did it rescue changes in cell or Golgi morphology that are predominantly controlled by the MT filaments themselves. By contrast, defects in HSV-1 and transferrin uptake and localization to the perinuclear space were rescued by the co-depletion of Kif5B, suggesting that the improper organization of detyrosinated MTs disrupts cargo sorting pathways by biasing MT-based transport toward outward-directed motors. This adds support to prior studies suggesting that kinesin-1 has a higher affinity for or activity on detyrosinated MTs (Cai et al., 2009; Dunn et al., 2008; Liao and Gundersen, 1998), including in the transport of transferrin (Lin et al., 2002). Moreover, our findings suggest that a critical function of TACC3 is to regulate the balance of dynamic and stable MTs in interphase cells, which affects cell shape and the motor-based transport of cargoes.

STAR★METHODS

LEAD CONTACT AND MATERIALS AVAILABILITY

Further information and requests for resources and reagents should be directed to and will be fulfilled by the Lead Contact, Derek Walsh (derek.walsh@northwestern.edu). All unique/stable reagents generated in this study are available from the Lead Contact without restriction.

EXPERIMENTAL MODEL AND SUBJECT DETAILS

Cell lines—Certified Primary Normal Human Dermal Fibroblasts isolated from human male neonatal foreskin (NHDFs, Lonza CC-2509), Phoenix-AMPHO (ATCC), Vero and BSC40 cells (Dr. Ian Mohr, NYU School of Medicine) were cultured in Dulbecco's Modified Eagle's Medium (DMEM) containing 5% Fetal Bovine Serum (FBS), 1% L-Glutamine, and 1% penicillin-streptomycin. SK-N-SHs (Dr. Patricia Spear, Northwestern University, Chicago, IL), originally isolated from a female with neuroblastoma, were cultured in DMEM containing 10% FBS, 1% L-Glutamine, and 1% penicillin-streptomycin. All cells were maintained at 37°C, 5% CO_2. For all experiments, low passage NHDF (less than passage 25) or SK-N-SH (less than passage 7) cells were used. NHDFs stably expressing eGFP-CLIP170 were described previously (Procter et al., 2018) and cultured as described above.

Virus strains—Wild-type HSV-1 strain F and HSV-1 K26GFP (Dr. Prashant Desai, Johns Hopkins University, Baltimore, MD) were propagated by infecting Vero cells in DMEM containing 1% FBS, 1% l-glutamine, and 1% penicillin-streptomycin (Desai and Person, 1998; Naghavi et al., 2013). Once > 90% cytopathic effect was observed, infected cells were scraped into culture medium and lysed by three rounds of freeze-thawing. Cell debris was removed by centrifugation. Virus was titrated by serial dilution and infection of Vero cells, followed by plaque counting. Vesicular Stomatitis Virus (VSV) was grown and titrated on BSC40 cells as described previously (Malikov et al., 2015).

METHOD DETAILS

siRNAs and plasmids—siRNAs used in this study were obtained from Thermo Fisher Scientific: control (Cat# AM4635), EB1 (3891), EB2 (21079, 136575), EB3 (19984), CLIP-170 (142517), TACC3 (135672, 3056), KIF5A (s7837), KIF5B (s731), KIF5C (s7842). For siRNA transfections, SK-N-SHs cells were plated in a 6-well plate and transfected the next day at 60% confluency with 150 pmol/ml siRNA using RNAiMax (Thermo Fisher Scientific). Efficient knockdown of protein levels in SK-N-SHs required a second round of siRNA treatment, 3 days after the first. Two days after this second treatment, cells were split into 12 well plates and the following day cells were infected or processed as described in the main text. For NHDFs, a single round of siRNA treatment with 150 pmol/ml siRNA for 3 days was sufficient for maximal knockdown, after which time cultures were infected or processed as described. For co-depletion experiments involving multiple siRNAs, 150 pmol/ml of each siRNA was used. All samples were treated with the same amount of siRNA, adjusting total amounts using control non-targeting siRNA. For plasmid transfections, the vector containing GFP-tagged TACC3 (pBRAIN-GFP-TACC3-KDP-shTACC3, obtained from Stephen Royle via Addgene) was transfected or electroporated into cells as described below. To generate FLAG-tagged TACC3, human TACC3 was PCR amplified from pBRAIN-GFP-TACC3-KDP-shTACC3 using the following primers containing AgeI and BamHI restriction sites:

Forward: 5′GCAACCGGTGCCACCATGGACTACAAAGACGATGACGACAAGAGTCTGCAGGTCTTAAAC 3′

Reverse: 5′GCAGGATCCTTATCTAGAGATCTTCTC 3′

To generate untagged TACC3, human TACC3 was PCR amplified using the following primers containing NotI and AgeI restriction sites:

Forward: 5′GCAGCGGCCGCGCCACCATGAGTCTGCAGGTCTTAAAC 3′

Reverse: 5′GCAACCGGTTTAGATCTTCTCCATCTTGGA 3′

The PCR product was purified, digested and ligated into the retroviral vector pQCXIP (Clontech). All inserts were verified by sequencing at the Northwestern University Sequencing Core. For transient expression of GFP-TACC3 or Flag-TACC3 in cells, SK-N-SHs were transfected with 1 μg DNA using Lipofectamine 3000 (Thermo Fisher Scientific) and imaged or processed after 3 days. NHDFs were electroporated with 2 μg of DNA using Amaxa™ 4D-Nucleofector™ (Lonza) according to the manufacturers protocol for human dermal fibroblasts, and imaged or processed after 1 day. Retroviral vectors expressing untagged or FLAG-tagged forms of TACC3 were produced by transfecting Phoenix-Ampho cells with pQXCIP vectors described above. Cell culture medium was changed 1 day after transfection. Supernatant containing virus was collected 2 days post-transfection and filtered through a 0.45mM filter. For transient expression approaches, SK-N-SHs were transduced with retroviruses expressing FLAG-TACC3, untagged TACC3 or empty pQCXIP control, in the presence of polybrene to increase infection efficiency. Cells were washed in PBS and

fresh media without polybrene was added 5 h post transduction. In order to rescue TACC3 levels in siRNA-treated SK-N-SHs, cultures were split from a 6 well plate to a 12 well plate 1 day after the second round of siRNA transfection (described above). The following day, the SK-N-SHs were transduced with the indicated retroviral vectors. One day post transduction, the cells were treated or analyzed as described in the manuscript.

Chemicals and nocodazole treatments—Actinomycin D (MP Biomedicals) was used at a concentration of 1 μg/ml. Bafilomycin A1 (Sigma; B1793) was used at a concentration of 100 nM. Cells were treated with DMSO solvent control or 10 μM nocodazole for 3 hours to depolymerize MTs prior to infection. To limit effects to dynamic MTs, cells were treated with 500 nM nocodazole for 2 hours prior to infection. In all cases the total amount of DMSO present was equivalent in all samples. For infections, cells were then infected with HSV-1 at MOI 10 for 5 hours. Cells were then lysed and analyzed by western blotting as described below. For immunofluorescence, cells were seeded onto coverslips in a 12 well plate prior to nocodazole treatment. To image incoming virus particles through VP5 staining, it was first necessary to prevent de-novo production of VP5. To do this, 1 hour prior to infection the cells were treated with 1 μg/ml actinomycin D. Cells were then infected at MOI 20 for 4 hours and fixed in ice-cold methanol and stained with indicated antibodies. Cells were imaged as described below. For nocodazole washout assays, NHDFs or SK-N-SHs were seeded onto coverslips in a 12 well plate. The following day, 10 μM nocodazole was added for 6 hours to ensure complete depolymerization of MTs. After 6 hours, cells were washed with PBS and fresh medium was added to cells for the indicated times before fixing in ice-cold methanol. Fixed cells were then stained and imaged as described below and in the main text. The area of MT regrowth after nocodazole washout was determined using the ImageJ threshold area function. Identical thresholds were set across all conditions.

Western Blot analysis—For WB analysis, cells were lysed in Laemmli buffer (62.5 mM Tris-HCl at pH 6.8, 2% SDS, 10% glycerol, 0.7 M β-mercaptoethanol). Samples were then boiled for 3 min and resolved using a 10% SDS-PAGE gel. Gels were transferred onto nitrocellulose membranes at 57 V for 1 hour. Membranes were then blocked by rocking for 1 h at RT in 5% non-fat milk diluted in TBS containing 0.1% Tween (TBS-T). Blots were then rinsed in TBS-T and incubated with the indicated primary antibody diluted in 3% BSA/TBS-T overnight at 4°C. The following day, membranes were washed in TBS-T and incubated with appropriate HRP-conjugated secondary antibodies diluted in 5% milk/TBS-T for 1 h at RT. Membranes were then washed in TBS-T, incubated with Pierce ECL Western Blotting Substrate (Thermo Fisher Scientific), and exposed on X-ray film. Densitometry analysis was performed on scanned films using ImageJ Gel Analyzer. Adjusted relative density was calculated using β-actin as a loading control.

Fixed and Live Cell Microscopy—For all immunofluorescence (IF) experiments, cells were seeded onto glass coverslips in a 12 well plate. Prior to fixation, cells were quickly rinsed in PBS. Cells were then fixed in ice cold methanol for 7 minutes and rinsed in PBS. Samples were blocked for 1 hour at 37°C in PBS containing 10% FBS and 0.25% saponin, and then incubated overnight at 4°C with the indicated primary antibodies diluted in PBS containing 10% FBS and 0.025% saponin. Samples were then washed in PBS containing

0.025% saponin (wash buffer) three times for 5 minutes, and then incubated for 1 hour at RT with appropriate Alexa Fluor-conjugated secondary antibodies diluted in PBS containing 10% FBS and 0.025% saponin. Samples were then incubated with Hoechst 33342 (Thermo Fisher Scientific 62249) in wash buffer before two subsequent washes. The coverslips were then mounted on slides using FluorSave (EMD Millipore, 345789) and imaged by wide field microscopy using a Leica DMI6000B-AFC microscope. Cells were imaged using a 100x objective (HC PL APO 100 3 /1.44 NA oil), an ORCA-FLASH 4.0 cMOS camera, and MetaMorph software. Images were processed and analyzed using ImageJ software, with equivalent settings used for processing any given dataset. For time-lapse microscopy, cells were seeded onto four-compartment 35 mm glass-bottom dishes (Greiner Bio-One). Immediately before imaging, media was changed to Leibovitz's L-15 Medium without phenol red (Thermo Fisher Scientific) supplemented with 2 mM L-Glutamine and 5% FBS. Cells were then imaged using a Leica DMI6000B-AFC microscope with an environmental chamber (InVivo) at 37°C using a 100x objective. For confocal microscopy, images were acquired using a motorized spinning-disc confocal microscope (Leica DMI 6000B) with Yokogawa CSU-X1 A1 confocal head and confocal z stacks were acquired at 0.2 μm intervals. Maximum intensity Z-projections were generated using ImageJ software. For live cell video microscopy of viral particles, cells were infected with HSV-1 K26GFP at MOI 100 in L-15 medium. Cells were then immediately imaged at 1 s intervals for 4–5 minutes. To quantify virus particle motility, individual particles were manually tracked for at least 10 s. Virus particle displacement relative to the nucleus was calculated between first and last frame of the track.

$$\text{Virus Particle Displacement} = \sqrt{(x_{first} - x_{last})^2 + (y_{first} - y_{last})^2}$$

For live-cell analysis of GFP-CLIP170 or GFP-TACC3, cells were imaged at 500 ms intervals for 1 minute. For transferrin imaging, cells were incubated with 25 mg/ml Alexa Fluor 647-conjugated transferrin (Thermo Fisher Scientific) for 30 min at 37°C (Jovasevic et al., 2015). For fixed analysis, cells were fixed in ice-cold methanol, co-stained with the indicated antibodies and imaged as described above. For live-cell analysis, medium was changed to fresh L-15 medium prior to imaging. Images were acquired at 500 ms intervals for 30 s.

Image Analysis and Quantification—To quantify EB1 comet numbers in fixed cells, identical thresholds for EB1 staining were set across all conditions. The indicated number of cells were manually outlined using tyrosinated-tubulin staining. The number of comets within the outlined area was determined using the particle analysis function in ImageJ. For analyzing EB1 comet length in fixed cells, the line-scan function of ImageJ was used to measure fluorescence intensity of EB1 staining along individual microtubules. Line-scans were normalized and aligned in Excel prior to analysis (Procter et al., 2018). To quantify chTOG levels in the nuclei of fixed cells, the corrected total fluorescence intensity of nuclear chTOG was averaged across the indicated number of cells. To obtain corrected total fluorescence intensity, nuclei were manually outlined using Hoechst staining and these outlines were applied to corresponding images of chTOG staining. ImageJ was used to

calculate the integrated density and area of each outlined region, along with the mean gray value of background. The product of the mean gray value of the background and the area of each region was subtracted from the region's integrated density to give the corrected total fluorescence intensity.

$$\text{Corrected total fluorescence intensity} = Integrated\ Density - (Area \times mean\ grey\ value\ of\ background)$$

The same calculation was used to determine corrected total fluorescence intensity of cytoplasmic TACC3 (using whole cell area excluding area of Hoechst staining) and perinuclear transferrin (using a fixed circular area adjacent to the nucleus). The area of TGN46 staining was quantified using the ImageJ threshold area function. Identical thresholds were set across all conditions. To quantify cell diameter, a line was measured perpendicular to the nucleus from one cell edge to the other, using b-actin or overexposed acetylated-tubulin staining to determine cell bounds.

For analyzing HSV-1 infectivity in fixed cells by IF, two approaches were used. First, cells were infected with HSV-1 at MOI 20 for 4 hours. Fixed cells were stained for HSV-1 immediate early protein ICP4 along with Hoechst. Second, cells were treated with 1 μg/ml actinomycin D for 1 hour prior to infection to prevent de-novo production of HSV-1 capsid protein. Cells were then infected as described above and fixed at 4 hours post infection. Fixed cells were stained for VP5 and Hoechst. The indicated number of nuclei were assessed manually for ICP4-expression or VP5 accumulation at the nucleus relative to the control condition. To examine efficiency of virus entry, cells were infected with HSV-1 at MOI 30 for 30 and 60 minutes. Fixed cells were stained for HSV-1 glycoprotein gB and capsid protein VP5. As a control for visualizing virus prior to entry, cells were infected at MOI 30 for 1 hour at 4°C before being fixed and stained for gB and VP5. To quantify fraction of viral particles that had entered the cell, the number of green VP5 particles was divided by the total number of viral particles, which included both green VP5 particles and yellow (green VP5 and red gB colocalizing) particles.

Antibodies—The following antibodies were used for Western Blotting or IF analysis; Abcam: ICP4 (ab6514), ICP0 (ab6513), VSV-G (ab50549), TACC3 *for IF* (ab134154), Kif5A (ab5628), Kif5B (ab25715), Kif5C (ab5630), α-tubulin (ab18251), γ-tubulin (ab27074), de-tyrosinated-tubulin (ab48389); Cell signaling technologies: β-actin (3700), TACC3 *for western* (8069S), Flag for *IF* (15009), Millipore-Sigma: Flag M2 for *western and 1 IF* (F3165), TACC2 (07–228), acetylated tubulin (T6793), EB3 (AB6033); Life Technologies: EB1 (412100); Santa Cruz Biotechnology, Inc: CLIP-170 (sc-25613); Absea: EB2 (010614A11); Bethyl: Pericentrin (IHC-00264); Bio-Legend: chTOG (620401); Novus Biologicals: TACC1 (NBP189447); Bio-Rad: TGN46 (AHP500GT); Virusys: VP5 (HA018). Anti-gB antibody was a gift of Dr. Richard Longnecker (Northwestern University, USA). Anti-PABP antibody was a gift from Dr. Simon Morley (University of Sussex, Sussex, England, UK). Anti-tyrosinated-tubulin antibody was a gift from Dr. Gregg Gunderson (Columbia University, New York, NY).

QUANTIFICATION AND STATISTICAL ANALYSIS

Data were analyzed using GraphPad Prism 7 and results are shown as mean ± standard errors of the mean. Independent sample t tests were used to assess statistical significance, with p values less than 0.05 considered as significant. Number of biological replicates are indicated in the figure legends.

DATA AND CODE AVAILABILITY

All data are available upon request to the lead contact. This study did not generate or analyze any code.

Supplementary Material

Refer to Web version on PubMed Central for supplementary material.

ACKNOWLEDGMENTS

We thank Prashant Desai, Ian Mohr, Richard Longnecker, Simon Morley, Gregg Gundersen, and Vladimir Gelfand for reagents and comments. This work was supported by grants R01AI141470 and P01GM105536 from the NIH (to D.W.).

REFERENCES

Akhmanova A, and Steinmetz MO (2008). Tracking the ends: a dynamic protein network controls the fate of microtubule tips. Nat. Rev. Mol. Cell Biol 9, 309–322. [PubMed: 18322465]

Akhmanova A, and Steinmetz MO (2015). Control of microtubule organization and dynamics: two ends in the limelight. Nat. Rev. Mol. Cell Biol 16, 711–726. [PubMed: 26562752]

Baas PW, and Black MM (1990). Individual microtubules in the axon consist of domains that differ in both composition and stability. J. Cell Biol 111, 495–509. [PubMed: 2199458]

Ban R, Matsuzaki H, Akashi T, Sakashita G, Taniguchi H, Park SY, Tanaka H, Furukawa K, and Urano T (2009). Mitotic regulation of the stability of microtubule plus-end tracking protein EB3 by ubiquitin ligase SIAH-1 and Aurora mitotic kinases. J. Biol. Chem 284, 28367–28381. [PubMed: 19696028]

Biedler JL, Helson L, and Spengler BA (1973). Morphology and growth, tumorigenicity, and cytogenetics of human neuroblastoma cells in continuous culture. Cancer Res. 33, 2643–2652. [PubMed: 4748425]

Brady S (1993). Axonal Dynamics and Regeneration In Neuroregeneration, Gorio A, ed. (Raven Press), pp. 7–36.

Brouhard GJ, Stear JH, Noetzel TL, Al-Bassam J, Kinoshita K, Harrison SC, Howard J, and Hyman AA (2008). XMAP215 is a processive microtubule polymerase. Cell 132, 79–88. [PubMed: 18191222]

Cai D, McEwen DP, Martens JR, Meyhofer E, and Verhey KJ (2009). Single molecule imaging reveals differences in microtubule track selection between Kinesin motors. PLoS Biol. 7, e1000216. [PubMed: 19823565]

Chabin-Brion K, Marceiller J, Perez F, Settegrana C, Drechou A, Durand G, and Poüs C (2001). The Golgi complex is a microtubule-organizing organelle. Mol. Biol. Cell 12, 2047–2060. [PubMed: 11452002]

Chanez B, Gonçalves A, Badache A, and Verdier-Pinard P (2015). Eribulin targets a ch-TOG-dependent directed migration of cancer cells. Oncotarget 6, 41667–41678. [PubMed: 26497677]

Delaney MK, Malikov V, Chai Q, Zhao G, and Naghavi MH (2017). Distinct functions of diaphanous-related formins regulate HIV-1 uncoating and transport. Proc. Natl. Acad. Sci. USA 114, E6932–E6941. [PubMed: 28760985]

Desai P, and Person S (1998). Incorporation of the green fluorescent protein into the herpes simplex virus type 1 capsid. J. Virol. 72, 7563–7568. [PubMed: 9696854]

Ding ZM, Huang CJ, Jiao XF, Wu D, and Huo LJ (2017). The role of TACC3 in mitotic spindle organization. Cytoskeleton (Hoboken) 74, 369–378. [PubMed: 28745816]

Dixit R, Barnett B, Lazarus JE, Tokito M, Goldman YE, and Holzbaur ELF (2009). Microtubule plus-end tracking by CLIP-170 requires EB1. Proc. Natl. Acad. Sci. USA 106, 492–497. [PubMed: 19126680]

Dunn S, Morrison EE, Liverpool TB, Molina-París C, Cross RA, Alonso MC, and Peckham M (2008). Differential trafficking of Kif5c on tyrosinated and detyrosinated microtubules in live cells. J. Cell Sci 121, 1085–1095. [PubMed: 18334549]

Erdogan B, Cammarata GM, Lee EJ, Pratt BC, Francl AF, Rutherford EL, and Lowery LA (2017). The microtubule plus-end-tracking protein TACC3 promotes persistent axon outgrowth and mediates responses to axon guidance signals during development. Neural Dev. 12, 3. [PubMed: 28202041]

Ferreira JG, Pereira AJ, Akhmanova A, and Maiato H (2013). Aurora B spatially regulates EB3 phosphorylation to coordinate daughter cell adhesion with cytokinesis. J. Cell Biol. 201, 709–724. [PubMed: 23712260]

Gard DL, and Kirschner MW (1987). A microtubule-associated protein from Xenopus eggs that specifically promotes assembly at the plus-end. J. Cell Biol 105, 2203–2215. [PubMed: 2890645]

Gard DL, Becker BE, and Josh Romney S (2004). MAPping the eukaryotic tree of life: structure, function, and evolution of the MAP215/Dis1 family of microtubule-associated proteins. Int. Rev. Cytol 239, 179–272. [PubMed: 15464854]

Gergely F, Karlsson C, Still I, Cowell J, Kilmartin J, and Raff JW (2000). The TACC domain identifies a family of centrosomal proteins that can interact with microtubules. Proc. Natl. Acad. Sci. USA 97, 14352–14357. [PubMed: 11121038]

Gergely F, Draviam VM, and Raff JW (2003). The ch-TOG/XMAP215 protein is essential for spindle pole organization in human somatic cells. Genes Dev. 17, 336–341. [PubMed: 12569123]

Gordon J, Amini S, and White MK (2013). General overview of neuronal cell culture. Methods Mol. Biol. 1078, 1–8. [PubMed: 23975816]

Guesdon A, Bazile F, Buey RM, Mohan R, Monier S, Garcíaı RR, Angevin M, Heichette C, Wieneke R, Tampé R, et al. (2016). EB1 interacts with outwardly curved and straight regions of the microtubule lattice. Nat. Cell Biol. 18, 1102–1108. [PubMed: 27617931]

Gunzelmann J, Rüthnick D, Lin T-C, Zhang W, Neuner A, Jäkle U, and Schiebel E (2018). The microtubule polymerase Stu2 promotes oligomerization of the γ-TuSC for cytoplasmic microtubule nucleation. eLife 7, e39932. [PubMed: 30222109]

Gutiérrez-Caballero C, Burgess SG, Bayliss R, and Royle SJ (2015). TACC3-ch-TOG track the growing tips of microtubules independently of clathrin and Aurora-A phosphorylation. Biol. Open 4, 170–179. [PubMed: 25596274]

Hallak ME, Rodriguez JA, Barra HS, and Caputto R (1977). Release of tyrosine from tyrosinated tubulin. Some common factors that affect this process and the assembly of tubulin. FEBS Lett. 73, 147–150. [PubMed: 838053]

Honnappa S, Gouveia SM, Weisbrich A, Damberger FF, Bhavesh NS, Jawhari H, Grigoriev I, van Rijssel FJ, Buey RM, Lawera A, et al. (2009). An EB1-binding motif acts as a microtubule tip localization signal. Cell 138, 366–376. [PubMed: 19632184]

Howard J, and Hyman AA (2003). Dynamics and mechanics of the microtubule plus end. Nature 422, 753–758. [PubMed: 12700769]

Hussmann F, Drummond DR, Peet DR, Martin DS, and Cross RA (2016). Alp7/TACC-Alp14/TOG generates long-lived, fast-growing MTs by an unconventional mechanism. Sci. Rep. 6, 20653. [PubMed: 26864000]

Janke C, and Bulinski JC (2011). Post-translational regulation of the microtubule cytoskeleton: mechanisms and functions. Nat. Rev. Mol. Cell Biol 12, 773–786. [PubMed: 22086369]

Jánosi IM, Chrétien D, and Flyvbjerg H (2002). Structural microtubule cap: stability, catastrophe, rescue, and third state. Biophys. J 83, 1317–1330. [PubMed: 12202357]

Jovasevic V, Naghavi MH, and Walsh D (2015). Microtubule plus endassociated CLIP-170 initiates HSV-1 retrograde transport in primary human cells. J. Cell Biol 211, 323–337. [PubMed: 26504169]

Kinoshita K, Noetzel TL, Pelletier L, Mechtler K, Drechsel DN, Schwager A, Lee M, Raff JW, and Hyman AA (2005). Aurora A phosphorylation of TACC3/maskin is required for centrosome-dependent microtubule assembly in mitosis. J. Cell Biol 170, 1047–1055. [PubMed: 16172205]

Komarova Y, Lansbergen G, Galjart N, Grosveld F, Borisy GG, and Akhmanova A (2005). EB1 and EB3 control CLIP dissociation from the ends of growing microtubules. Mol. Biol. Cell 16, 5334–5345. [PubMed: 16148041]

Komarova Y, De Groot CO, Grigoriev I, Gouveia SM, Munteanu EL, Schober JM, Honnappa S, Buey RM, Hoogenraad CC, Dogterom M, et al. (2009). Mammalian end binding proteins control persistent microtubule growth. J. Cell Biol. 184, 691–706. [PubMed: 19255245]

Kreis TE (1987). Microtubules containing detyrosinated tubulin are less dynamic. EMBO J. 6, 2597–2606. [PubMed: 3315650]

Kristofferson D, Mitchison T, and Kirschner M (1986). Direct observation of steady-state microtubule dynamics. J. Cell Biol 102, 1007–1019. [PubMed: 3005332]

Kume K, Kaneko S, Nishikawa K, Mizunuma M, and Hirata D (2018). Role of nucleocytoplasmic transport in interphase microtubule organization in fission yeast. Biochem. Biophys. Res. Commun 503, 1160–1167. [PubMed: 29958883]

Lansbergen G, Grigoriev I, Mimori-Kiyosue Y, Ohtsuka T, Higa S, Kitajima I, Demmers J, Galjart N, Houtsmuller AB, Grosveld F, and Akhmanova A (2006). CLASPs attach microtubule plus ends to the cell cortex through a complex with LL5beta. Dev. Cell 11, 21–32. [PubMed: 16824950]

Lee MJ, Gergely F, Jeffers K, Peak-Chew SY, and Raff JW (2001). Msps/XMAP215 interacts with the centrosomal protein D-TACC to regulate microtubule behaviour. Nat. Cell Biol 3, 643–649. [PubMed: 11433296]

Liao G, and Gundersen GG (1998). Kinesin is a candidate for cross-bridging microtubules and intermediate filaments. Selective binding of kinesin to detyrosinated tubulin and vimentin. J. Biol. Chem. 273, 9797–9803. [PubMed: 9545318]

Liao G, Nagasaki T, and Gundersen GG (1995). Low concentrations of nocodazole interfere with fibroblast locomotion without significantly affecting microtubule level: implications for the role of dynamic microtubules in cell locomotion. J. Cell Sci. 108, 3473–3483. [PubMed: 8586659]

Lin SX, Gundersen GG, and Maxfield FR (2002). Export from pericentriolar endocytic recycling compartment to cell surface depends on stable, detyrosinated (glu) microtubules and kinesin. Mol. Biol. Cell 13, 96–109. [PubMed: 11809825]

Lin C-H, Hu C-K, and Shih H-M (2010). Clathrin heavy chain mediates TACC3 targeting to mitotic spindles to ensure spindle stability. J. Cell Biol 189, 1097–1105. [PubMed: 20566684]

Ling YC, Vjestica A, and Oliferenko S (2009). Nucleocytoplasmic shuttling of the TACC protein Mia1p/Alp7p is required for remodeling of microtubule arrays during the cell cycle. PLoS One 4, e6255. [PubMed: 19606211]

Long JB, Bagonis M, Lowery LA, Lee H, Danuser G, and Van Vactor D (2013). Multiparametric analysis of CLASP-interacting protein functions during interphase microtubule dynamics. Mol. Cell. Biol 33, 1528–1545. [PubMed: 23382075]

Malikov V, da Silva ES, Jovasevic V, Bennett G, de Souza Aranha Vieira DA, Schulte B, Diaz-Griffero F, Walsh D, and Naghavi MH (2015). HIV-1 capsids bind and exploit the kinesin-1 adaptor FEZ1 for inward movement to the nucleus. Nat. Commun. 6, 6660. [PubMed: 25818806]

Maurer SP, Fourniol FJ, Bohner G, Moores CA, and Surrey T (2012). EBs recognize a nucleotide-dependent structural cap at growing microtubule ends. Cell 149, 371–382. [PubMed: 22500803]

McKenney RJ, Huynh W, Vale RD, and Sirajuddin M (2016). Tyrosination of α-tubulin controls the initiation of processive dynein-dynactin motility. EMBO J. 35, 1175–1185. [PubMed: 26968983]

Mortuza GB, Cavazza T, Garcia-Mayoral MF, Hermida D, Peset I, Pedrero JG, Merino N, Blanco FJ, Lyngsø J, Bruix M, et al. (2014). XTACC3-XMAP215 association reveals an asymmetric interaction promoting microtubule elongation. Nat. Commun. 5, 5072. [PubMed: 25262927]

Naghavi MH, and Walsh D (2017). Microtubule Regulation and Function during Virus Infection. J. Virol. 91, e00538–17. [PubMed: 28615197]

Naghavi MH, Gundersen GG, and Walsh D (2013). Plus-end tracking proteins, CLASPs, and a viral Akt mimic regulate herpesvirus-induced stable microtubule formation and virus spread. Proc. Natl. Acad. Sci. USA 110, 18268–18273. [PubMed: 24145430]

Nakamura S, Grigoriev I, Nogi T, Hamaji T, Cassimeris L, and Mimori-Kiyosue Y (2012). Dissecting the nanoscale distributions and functions of microtubule-end-binding proteins EB1 and ch-TOG in interphase HeLa cells. PLoS One 7, e51442. [PubMed: 23251535]

Nakaseko Y, Goshima G, Morishita J, and Yanagida M (2001). M phasespecific kinetochore proteins in fission yeast: microtubule-associating Dis1 and Mtc1 display rapid separation and segregation during anaphase. Curr. Biol 11, 537–549. [PubMed: 11369198]

Nwagbara BU, Faris AE, Bearce EA, Erdogan B, Ebbert PT, Evans MF, Rutherford EL, Enzenbacher TB, and Lowery LA (2014). TACC3 is a microtubule plus end-tracking protein that promotes axon elongation and also regulates microtubule plus end dynamics in multiple embryonic cell types. Mol. Biol. Cell 25, 3350–3362. [PubMed: 25187649]

Peset I, and Vernos I (2008). The TACC proteins: TACC-ling microtubule dynamics and centrosome function. Trends Cell Biol. 18, 379–388. [PubMed: 18656360]

Portran D, Schaedel L, Xu Z, Théry M, and Nachury MV (2017). Tubulin acetylation protects long-lived microtubules against mechanical ageing. Nat. Cell Biol. 19, 391–398. [PubMed: 28250419]

Procter DJ, Banerjee A, Nukui M, Kruse K, Gaponenko V, Murphy EA, Komarova Y, and Walsh D (2018). The HCMV Assembly Compartment Is a Dynamic Golgi-Derived MTOC that Controls Nuclear Rotation and Virus Spread. Dev. Cell 45, 83–100.e7. [PubMed: 29634939]

Raff JW (2002). Centrosomes and cancer: lessons from a TACC. Trends Cell Biol. 12, 222–225. [PubMed: 12062169]

Rodrĭguez JA, Arce CA, Barra HS, and Caputto R (1973). Release of tyrosine incorporated as a single unit into rat brain protein. Biochem. Biophys. Res. Commun 54, 335–340. [PubMed: 4741571]

Roizman B, Knipe DM, and Whitley R (2013). Herpes simplex viruses In Fields Virology, Knipe DM and Howley PM, eds. (Wolters Kluwer/Lippincott Williams & Wilkins Health), pp. 1823–1897.

Sabo Y, Walsh D, Barry DS, Tinaztepe S, de Los Santos K, Goff SP, Gundersen GG, and Naghavi MH (2013). HIV-1 induces the formation of stable microtubules to enhance early infection. Cell Host Microbe 14, 535–546. [PubMed: 24237699]

Sahenk Z, and Brady ST (1987). Axonal tubulin and microtubules: morphologic evidence for stable regions on axonal microtubules. Cell Motil. Cytoskeleton 8, 155–164. [PubMed: 2891447]

Sato M, and Toda T (2007). Alp7/TACC is a crucial target in Ran-GTPasedependent spindle formation in fission yeast. Nature 447, 334–337. [PubMed: 17476213]

Sato M, Vardy L, Angel Garcia M, Koonrugsa N, and Toda T (2004). Interdependency of fission yeast Alp14/TOG and coiled coil protein Alp7 in microtubule localization and bipolar spindle formation. Mol. Biol. Cell 15, 1609–1622. [PubMed: 14742702]

Sato M, Okada N, Kakui Y, Yamamoto M, Yoshida M, and Toda T (2009). Nucleocytoplasmic transport of Alp7/TACC organizes spatiotemporal microtubule formation in fission yeast. EMBO Rep. 10, 1161–1167. [PubMed: 19696784]

Slep KC, and Vale RD (2007). Structural basis of microtubule plus end tracking by XMAP215, CLIP-170, and EB1. Mol. Cell 27, 976–991. [PubMed: 17889670]

Song Y, Kirkpatrick LL, Schilling AB, Helseth DL, Chabot N, Keillor JW, Johnson GV, and Brady ST (2013). Transglutaminase and polyamination of tubulin: posttranslational modification for stabilizing axonal microtubules. Neuron 78, 109–123. [PubMed: 23583110]

Stephens DJ (2012). Functional coupling of microtubules to membranes - implications for membrane structure and dynamics. J. Cell Sci. 125, 2795–2804. [PubMed: 22736043]

Still IH, Vince P, and Cowell JK (1999). The third member of the transforming acidic coiled coil-containing gene family, TACC3, maps in 4p16, close to translocation breakpoints in multiple myeloma, and is upregulated in various cancer cell lines. Genomics 58, 165–170. [PubMed: 10366448]

Still IH, Vettaikkorumakankauv AK, DiMatteo A, and Liang P (2004). Structure-function evolution of the transforming acidic coiled coil genes revealed by analysis of phylogenetically diverse organisms. BMC Evol. Biol. 4, 16. [PubMed: 15207008]

Thakur HC, Singh M, Nagel-Steger L, Kremer J, Prumbaum D, Fansa EK, Ezzahoini H, Nouri K, Gremer L, Abts A, et al. (2014). The centrosomal adaptor TACC3 and the microtubule polymerase chTOG interact via defined C-terminal subdomains in an Aurora-A kinase-independent manner. J. Biol. Chem. 289, 74–88. [PubMed: 24273164]

Trogden KP, and Rogers SL (2015). TOG Proteins Are Spatially Regulated by Rac-GSK3b to Control Interphase Microtubule Dynamics. PLoS One 10, e0138966. [PubMed: 26406596]

Xie S, Bahl K, Reinecke JB, Hammond GRV, Naslavsky N, and Caplan S (2016). The endocytic recycling compartment maintains cargo segregation acquired upon exit from the sorting endosome. Mol. Biol. Cell 27, 108–126. [PubMed: 26510502]

Xu Z, Schaedel L, Portran D, Aguilar A, Gaillard J, Marinkovich MP, Théry M, and Nachury MV (2017). Microtubules acquire resistance from mechanical breakage through intralumenal acetylation. Science 356, 328–332. [PubMed: 28428427]

Zhang R, Alushin GM, Brown A, and Nogales E (2015). Mechanistic Origin of Microtubule Dynamic Instability and Its Modulation by EB Proteins. Cell 162, 849–859. [PubMed: 26234155]

Zheng L, Schwartz C, Wee L, and Oliferenko S (2006). The fission yeast transforming acidic coiled coil-related protein Mia1p/Alp7p is required for formation and maintenance of persistent microtubule-organizing centers at the nuclear envelope. Mol. Biol. Cell 17, 2212–2222. [PubMed: 16481403]

Highlights

- TACC3 regulates microtubule plus-end growth and HSV-1 infection in interphase cells
- Loss of TACC3 functionality results in aberrant detyrosinated microtubule arrays
- Effects of TACC3 on stable microtubule arrays affect cell shape and cargo sorting
- Cargo sorting defects caused by TACC3 loss are rescued by impairing kinesin-1 activity

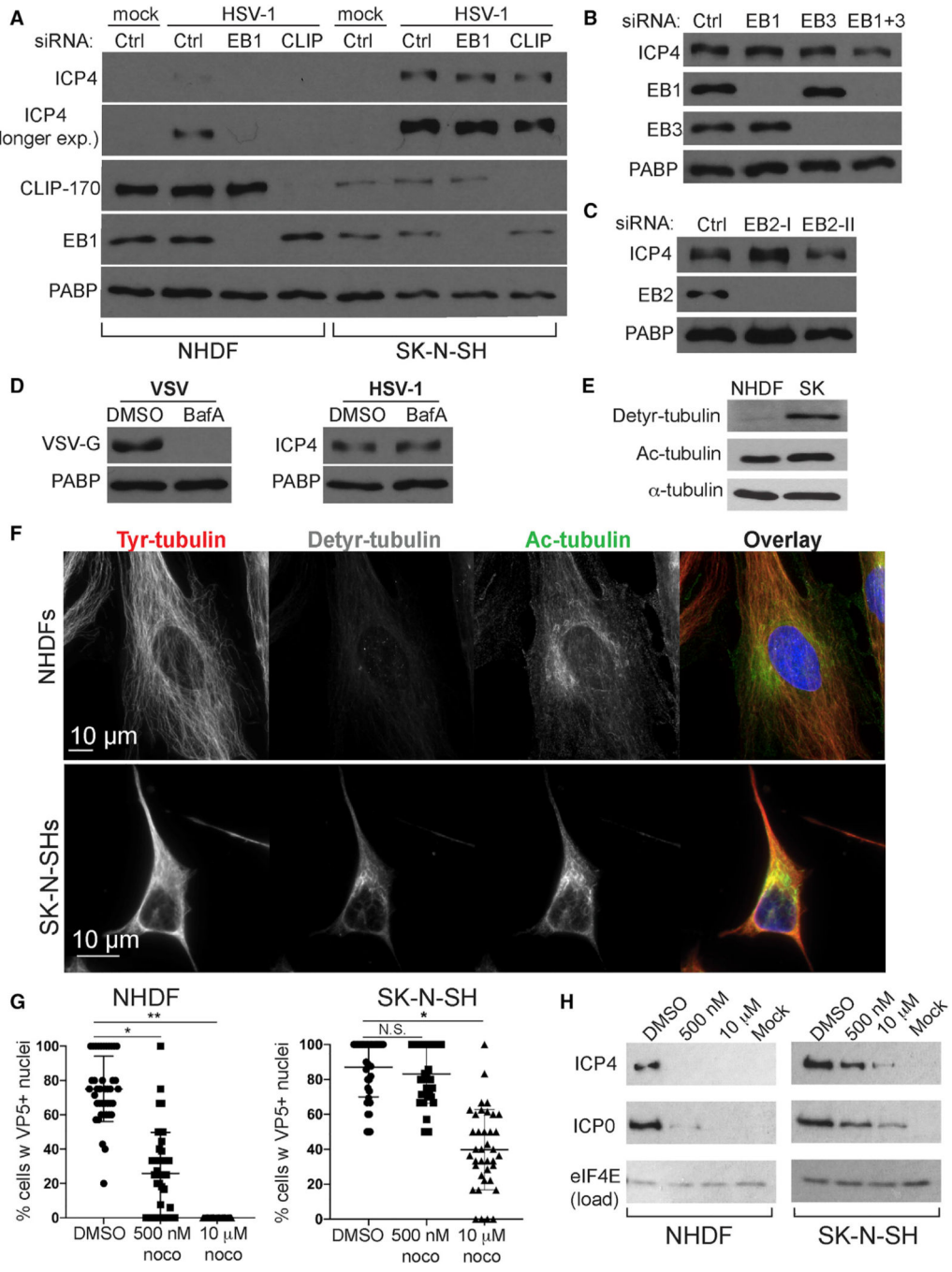

Figure 1. Stable MTs Mediate EB-Independent HSV-1 Infection of SK-N-SHs

(A) NHDFs or SK-N-SHs treated with non-targeting (ctrl), EB1, or CLIP-170 (CLIP) siRNAs were mock-infected or infected with HSV-1 at MOI 10 for 5 h and analyzed by WB.

(B) SK-N-SHs treated with the indicated siRNAs were infected, as in (A).

(C) SK-N-SHs treated with independent EB2 siRNAs (I or II) were infected, as in (A).

(D) SK-N-SHs were treated with 100 nM BafA or DMSO and infected at MOI 10 with VSV for 4 h or HSV-1 for 5 h.

(E) NHDFs or SK-N-SHs analyzed by WB using the indicated antibodies.

(F) NHDFs or SK-N-SHs stained for tyrosinated (Tyr), detyrosinated (Detyr), and acetylated (Ac) tubulin. Nuclei were stained with Hoechst.

(G) NHDFs or SK-N-SHs treated with 500 nM DMSO or 10 μM nocodazole were infected at MOI 20 with HSV-1 for 4 h in the presence of 1 μg/mL actinomycin D. Fixed cells were stained for VP5 and with Hoechst. Assessed for the accumulation of VP5 over 2 biological replicates were ≥ 165 NHDF or ≥ 190 SK-N-SH nuclei; error bars, SEMs; *$p < 0.05$, **$p < 0.01$, N.S., not significant; unpaired 2-tailed t test.

(H) Cells treated as in (G) were infected at MOI 10 with HSV-1 for 5 h.

All of the experiments represent ≥3 replicates unless indicated. See also Figures S1 and S2.

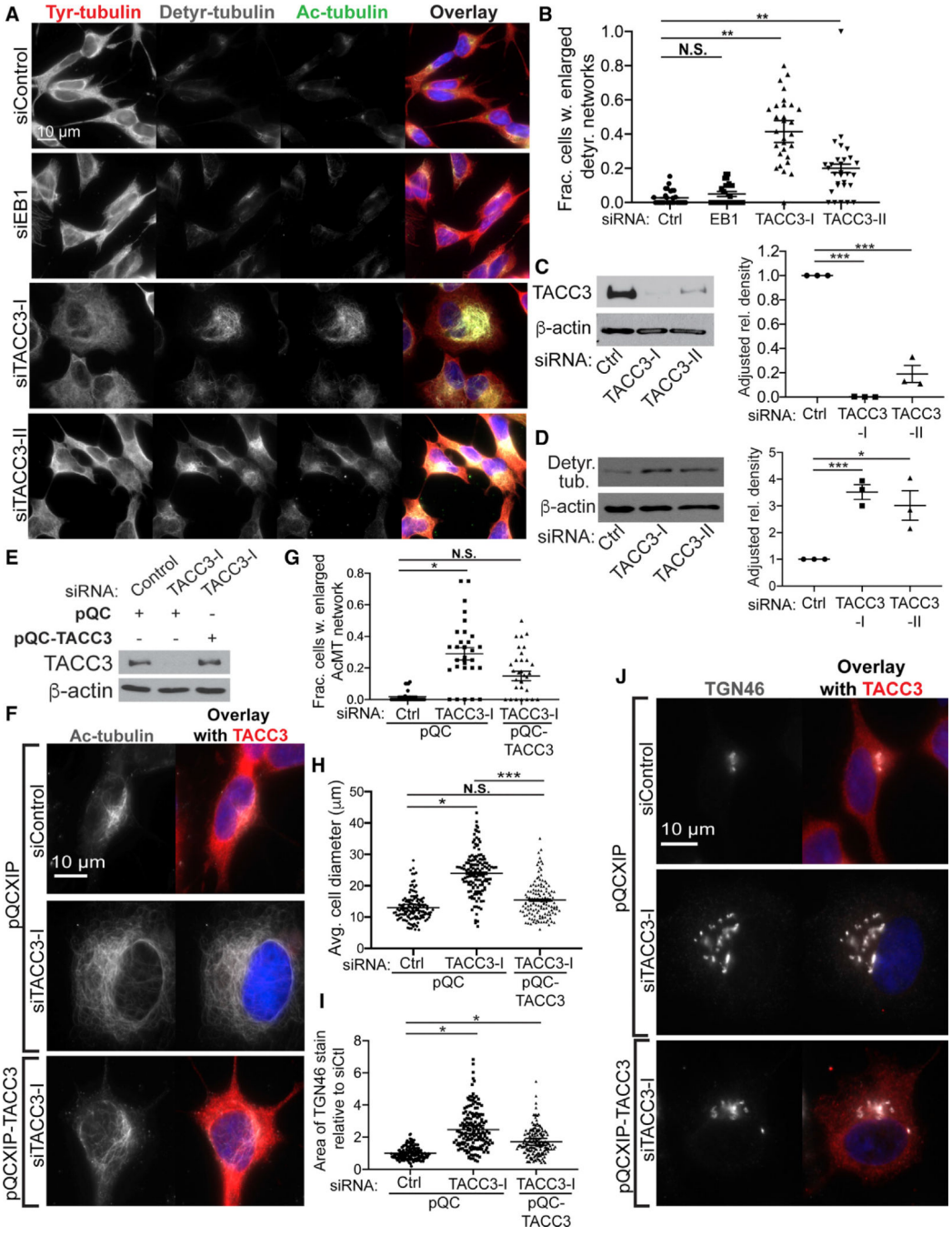

Figure 2. TACC3 Regulates Stable MTs and Cell Diameter

(A) SK-N-SHs treated with control, TACC3 (I or II), or EB1 siRNAs were fixed and stained for tyrosinated (Tyr) tubulin (red), detyrosinated (Detyr) tubulin (gray), or acetylated (Ac) tubulin (green). Nuclei were stained with Hoechst.

(B) Average fraction of SK-N-SHs treated as in (A), with highly enlarged Detyr-MT networks; ≥ 170 cells per siRNA over 2 biological replicates; error bars, SEMs; **p < 0.01, N.S., not significant; unpaired 2-tailed t test.

(C) SK-N-SHs were treated with the indicated siRNAs. Average adjusted relative density (AU) of TACC3 was quantified across 3 separate WBs; error bars, SEMs; ***p < 0.005; unpaired 2-tailed t test.

(D) SK-N-SHs were treated with the indicated siRNAs. AU of detyrosinated tubulin was quantified across 3 separate WBs; error bars, SEMs; *p < 0.05,***p < 0.005; unpaired 2-tailed t test.

(E) SK-N-SHs were treated with the indicated siRNAs, transduced with either pQCXIP (pQC) or pQCXIP-TACC3 (pQC-TACC3) retroviral vectors, and analysed by WB.

(F) Cells treated as in (E) were fixed and stained for TACC3 (red) and acetylated tubulin (gray). Nuclei were stained using Hoechst.

(G) Average fraction of SK-N-SHs with highly enlarged acetylated MT networks; ≥ 250 cells per condition over 2 biological replicates; error bars, SEMs; *p < 0.05, N.S., not significant; unpaired 2-tailed t test.

(H) Average cell diameter taken perpendicular to the nucleus; ≥ 130 cells per condition over 2 biological replicates; error bars, SEMs; *p < 0.05, ***p < 0.005, N.S., not significant; unpaired 2-tailed t test.

(I and J) Cells treated as in (E) were fixed and stained for TACC3 (red) and TGN46 (gray).

(I) Average area of TGN46 staining in SK-N-SHs treated as in (E); ≥ 160 cells per condition over 2 biological replicates; error bars, SEMs; *p < 0.05; unpaired 2-tailed t test.

(J) Representative images for each condition.

See also Figure S3.

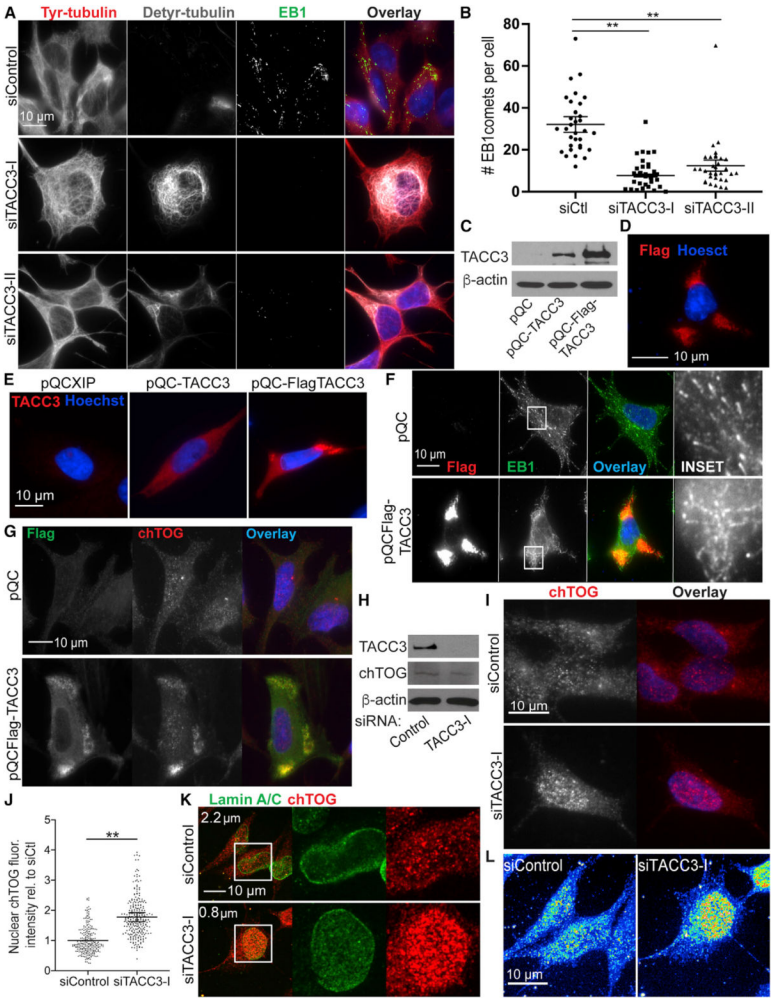

Figure 3. TACC3 Regulates MT Dynamics and chTOG Localization

(A) SK-N-SHs were treated with siRNAs and then fixed and stained for tyrosinated (Tyr) and detyrosinated (Detyr) tubulin, EB1, and Hoechst. Representative cells are shown.

(B) Average number of EB1 comets per cell treated as in (A). Total number of EB1 comets in 30 cells per siRNA over 3 biological replicates; error bars, SEMs; **p < 0.01; unpaired 2-tailed t test.

(C) SK-N-SHs were transduced with pQC, pQC-TACC3, or pQCXIP-FLAG-TACC3 (pQC-FLAG-TACC3) retroviral vectors and analyzed by WB.

(D) SK-N-SHs transfected with pQC-FLAGTACC3 and fixed and stained for FLAG and with Hoechst.

(E) SK-N-SHs transduced as in (C) were fixed and stained for TACC3 and Hoechst.

(F) SK-N-SHs were transfected with pQC or pQC-FLAG-TACC3, fixed after 3 days, and stained for FLAG (red), EB1 (green), and with Hoechst. Enlarged image shows elongated EB1 staining patterns, indicative of reduced MT polymerization, in cells expressing FLAG-TACC3.

(G) SK-N-SHs as in (F) were fixed and stained for FLAG (green) and chTOG (red) and with Hoechst.

(H) SK-N-SHs treated with control or TACC3 siRNA and analyzed by WB.

(I) siRNA-treated SK-N-SHs fixed and stained for chTOG (red) and with Hoechst.
(J) Average corrected total fluorescence intensity of nuclear chTOG in SK-N-SHs treated with siRNAs; ≥ 255 cells per siRNA over 3 biological replicates; error bars, SEMs; **$p < 0.01$; unpaired 2-tailed t test.
(K) SK-N-SHs were treated with siRNAs, fixed and stained for lamin A/C (green) and chTOG (red), and imaged by confocal microscopy. A still from Video S2 is shown.
(L) Maximum intensity projection of chTOG from confocal z stack in (K). A color-intensity heatmap is shown.
See also Figures S4, S5, and S6.

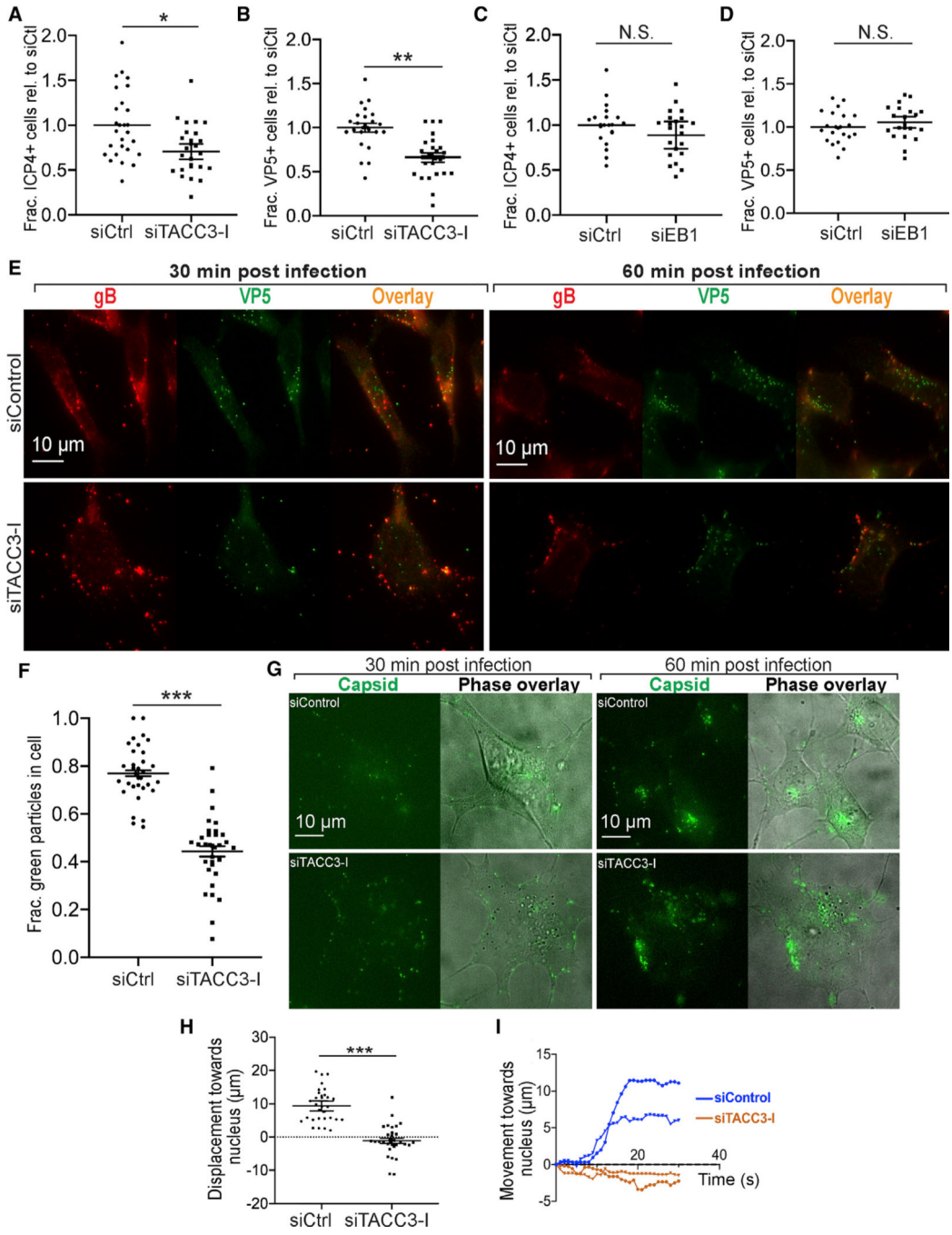

Figure 4. TACC3 Regulates HSV-1 Infection

(A and B) SK-H-SHs treated with control or TACC3 siRNA and infected at MOI 20 for 4 h. Nuclei were stained and assessed for (A) ICP4 expression or (B) VP5 capsid accumulation; ≥ 275 cells per siRNA over 2 biological replicates; error bars, SEMs; *p < 0.05, **p < 0.01; unpaired 2-tailed t test.

(C and D) SK-N-SHs were treated with control or EB1 siRNA (from Figure 1A) and infected with HSV-1, fixed, and stained as in (A) and (B). ICP4 expression in the nucleus

(C) and VP5 accumulation at the nuclear rim (D) were quantified as above; R330 cells per siRNA over 2 biological replicates; error bars, SEMs; N.S., not significant; 2-tailed t test.
(E) SK-N-SH were treated with control or TACC3 siRNA and infected with HSV-1 at MOI 30 for 30 or 60 min. Cells were stained for gB (red) and VP5 (green).
(F) SK-N-SHs treated and stained as in (E), fixed at 30 min post-infection. Average fraction of green particles versus green and yellow particles per cell was quantified. Thirty cells per siRNA were analyzed over 3 biological replicates; error bars, SEMs; ***$p < 0.005$; unpaired 2-tailed t test.
(G) Still images from Video S3 of siRNA-treated SK-N-SH infected with HSV-1 K26GFP at MOI 100. Cells were imaged at 30 and 60 min post-infection. Phase images show the infected cell.
(H) Individual virus particles from cells as in (G) were manually tracked for at least 10 s. For each track, the virus particle displacement relative to the nucleus was quantified. Thirty particles per siRNA were analyzed over 3 biological replicates; error bars, SEMs; ***$p < 0.005$; unpaired 2-tailed t test.
(I) Movement toward the nucleus of 2 representative particles for each siRNA in (H); blue, siControl-treated cells; orange, siTACC3-I-treated cells.
All of the experiments represent R3 replicates unless indicated. See also Figure S6.

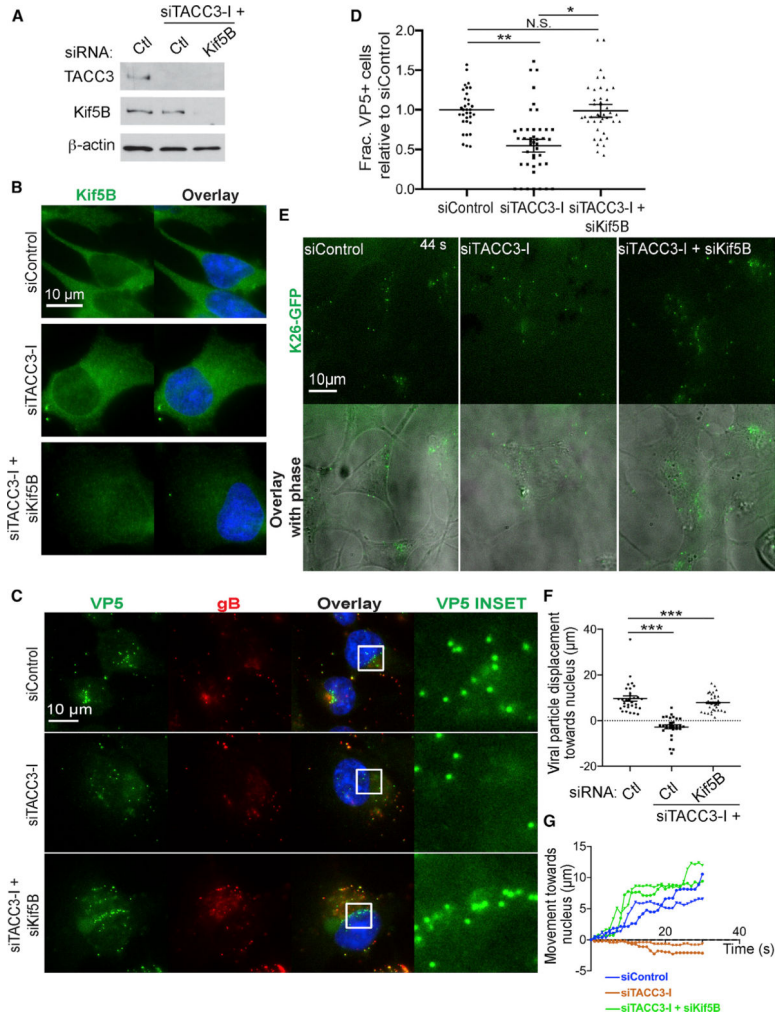

Figure 5. Kinesin-1 Prevents Perinuclear Accumulation of HSV-1 Particles in TACC3-Depleted SK-N-SHs

SK-N-SHs were treated with the indicated combination of siRNAs.

(A) Cells were analyzed by WB using the indicated antibodies.

(B) Cells were fixed and stained for Kif5B (green) along with Hoechst.

(C) Cells were infected with HSV-1 at MOI 20 for 4 h. Fixed cells were stained for VP5 (green) and gB (red) along with Hoechst. Inset shows enlarged view of VP5 at the perinuclear space.

(D) VP5 capsid accumulation at nucleus in SK-N-SHs treated and infected as in (C); R225 cells per siRNA over 3 biological replicates; error bars, SEMs; *$p < 0.05$, **$p < 0.01$, N.S., not significant; unpaired 2-tailed t test.

(E) Still images from Video S4 of siRNA-treated SK-N-SHs infected with HSV-1 K26GFP at MOI 100 and imaged by time-lapse fluorescence microscopy at 60 min post-infection to visualize GFP-tagged capsid. Phase images show the infected cell.

(F) Individual virus particles from cells as in (E) were manually tracked for at least 10 s. For each track, virus particle displacement relative to the nucleus was quantified. Thirty particles per siRNA were analyzed over 3 biological replicates; error bars, SEMs; ***$p < 0.005$; unpaired 2-tailed t test.

(G) Movement toward the nucleus of 2 individual particles as in (F) from each siRNA treatment, color-coded as indicated.

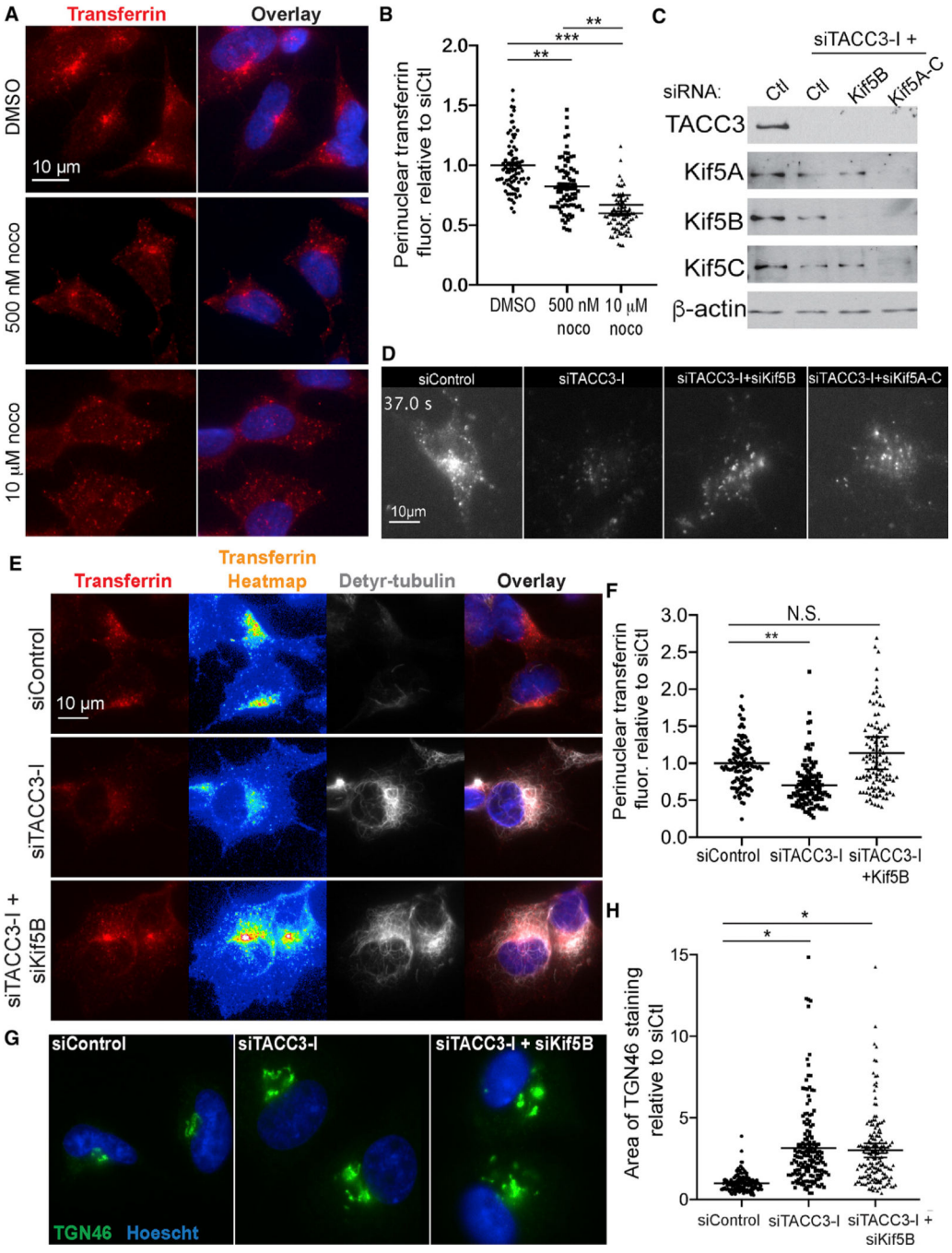

Figure 6. Kinesin-1 Prevents Perinuclear Accumulation of Transferrin in TACC3-Depleted SK-N-SHs

(A) SK-N-SHs were treated with DMSO or 10 μM nocodazole for 3 h or 500 nM nocodazole for 2 h. Cells were then incubated with Alexa Fluor 647-transferrin for 30 min and fixed. Nuclei were stained with Hoechst.

(B) Average corrected total fluorescence intensity of perinuclear transferrin; ≥ 80 cells per siRNA counted over 2 biological replicates; error bars, SEMs; **p < 0.01, ***p < 0.005; unpaired 2-tailed t test.

(C) SK-N-SHs were treated with the indicated combination of siRNAs and analyzed by WB.

(D) siRNA-treated SK-N-SHs were incubated with Alexa Fluor 647-transferrin for 30 min. Still image from Video S5 shows fluorescent transferrin accumulating in control or Kif5B and TACC3 co-depleted cells.

(E) SK-N-SHs treated with indicated siRNAs and incubated with transferrin as in (D) were fixed and stained for detyrosinated tubulin (Detyr; gray) along with Hoechst. Alexa Fluor 647-transferrin shown by color-intensity heatmap.

(F) Average corrected total fluorescence intensity of perinuclear transferrin; ≥ 110 cells per siRNA counted over 3 biological replicates; error bars, SEMs; **$p < 0.01$, N.S., not significant; unpaired 2-tailed t test.

(G) SK-N-SHs treated with the indicated siRNAs were fixed and stained for TGN46 (green) along with Hoechst.

(H) Average area of TGN46 staining in SK-N-SHs as in (G), relative to siControl; ≥ 160 cells per condition over 2 biological replicates; error bars, SEMs; *$p < 0.05$; unpaired 2-tailed t test.

KEY RESOURCES TABLE

REAGENT or RESOURCE	SOURCE	IDENTIFIER
Antibodies		
Anti-HSV-1 ICP4 Immediate Early Protein [10F1], mouse monoclonal	Abcam	Cat# ab6514; RRID:AB_305537
Anti-HSV-1 ICP0 [5H7], mouse monoclonal	Abcam	Cat# ab6513; RRID:AB_305536
Anti-VSV-G tag [P5D4], mouse monoclonal	Abcam	Cat# ab50549; RRID:AB_883494
Anti-TACC3 [EPR7756], rabbit monoclonal	Abcam	Cat# ab134154
Anti-Kinesin-5C, rabbit polyclonal	Abcam	Cat# ab5630; RRID:AB_304999
Anti-alpha tubulin, rabbit polyclonal	Abcam	Cat# ab18251; RRID:AB_2210057
Anti-gamma tubulin antibody [TU-30]	Abcam	Cat# ab27074; RRID:AB_2211240
Anti-detyrosinated alpha tubulin, mouse monoclonal	Abcam	Cat# ab48389; RRID:AB_869990
Anti-beta actin [8H10D10], mouse monoclonal	Cell Signaling Technology	Cat# 3700
Anti-TACC3 [D9E4] XP *for western*, rabbit monoclonal	Cell Signaling Technology	Cat# 8069; RRID:AB_10830219
Anti-Flag DYKDDDDK Tag [D6W5B] *for IF*, rabbit monoclonal	Cell Signaling Technology	Cat# 15009; RRID:AB_2798687
Anti-FLAG® M2 *for western and 1 IF*, mouse monoclonal	MilliporeSigma	Cat# F3165; RRID:AB_259529
Anti-TACC2, rabbit polyclonal	MilliporeSigma	Cat# 07–228; RRID:AB_310448
Anti-EB1 [1A11/4], mouse monoclonal	Thermo Fisher Scientific	Cat# 41–2100; RRID:AB_2533500
Anti-Kif5A, rabbit polyclonal	Abcam	Cat# ab5628; RRID:AB_2132218
Anti-Kif5B, rabbit polyclonal	Abcam	Cat# ab25715; RRID:AB_2132381
Anti-tubulin, acetylated, mouse monoclonal	MilliporeSigma	Cat# T6793; RRID:AB_477585
Anti-CLIP-170 [H-300], rabbit polyclonal	Santa Cruz Biotechnology	Cat# sc-25613; RRID:AB_2082238
Anti-EB2 [KT52], mouse monoclonal	Absea	Cat# 010614A11
Anti-EB3, rabbit polyclonal	MilliporeSigma	Cat# AB6033; RRID:AB_10806097
Anti-pericentrin/kendrin IHC, rabbit polyclonal	Bethyl	Cat# IHC-00264; RRID:AB_961069
Anti-chTOG, rabbit polyclonal	BioLegend	Cat# 620401; RRID:AB_2080729
Anti-TACC1, rabbit	Novus	Cat# NBP1–89447; RRID:AB_11013056
Anti-Human TGN46, sheep polyclonal	BioRad	Cat# AHP500GT; RRID:AB_2203291

REAGENT or RESOURCE	SOURCE	IDENTIFIER
Anti-HSV ICP5, mouse monoclonal	Virusys Corporation	Cat# HA018; RRID:AB_2713935
Anti-gB, rabbit	Dr. Richard Longnecker (Northwestern University, Chicago, IL, USA)	N/A
Anti-PAPB, rabbit polyclonal	Dr. Simon Morley (University of Sussex, Sussex, England, UK)	N/A
Anti-tyrosinated tubulin, rat	Dr. Gregg Gunderson (Columbia University, New York, NY, USA)	N/A
Bacterial and Virus Strains		
retroviral vector: pBABE-puro-AA-GFP-CLIP-170	Dr. Derek Walsh (Northwestern University, Chicago, IL, USA)	Procter et al., 2018
retroviral vector: pQCXIP-TACC3	This paper	N/A
retroviral vector: pQCXIP-FLAG-TACC3	This paper	N/A
retroviral vector: pQCXIP	Clontech	Cat# 631516
Escherichia coli (*E. coli*) DH5α strain	Thermo Fisher Scientific	Cat# 18265017
HSV-1 (F strain)	Dr. Ian Mohr (NYU-Lagone, New York, NY, USA)	N/A
HSV-1 K26GFP	Dr. Prashant Desai (Johns Hopkins University, Baltimore, MD, USA)	N/A
VSV (Indiana Strain)	Dr. Ian Mohr (NYU-Lagone, New York, NY, USA)	N/A
Chemicals, Peptides, and Recombinant Proteins		
Lipofectamine 3000 Transfection Reagent	Thermo Fisher Scientific	L3000015
Amaxa™ P2 Primary Cell 4D-Nucleofector™ X Kit L	Lonza	Cat# V4XP-2024
Polybrene	Santa Cruz Biotechnology	Cat# sc-134220
FluroSave Reagent	MilliporeSigma	Cat# 345789
Hoechst 33342	Thermo Fisher Scientific	Cat# 62249
Actinomycin D	MP Biomedicals	Cat# 0210465801

REAGENT or RESOURCE	SOURCE	IDENTIFIER
Bafilomycin A1	MilliporeSigma	Cat# B1793
Nocodazole	MilliporeSigma	M1404
Lipofectamine RNAiMAX Transfection Reagent	Thermo Fisher Scientific	13778030
Experimental Models: Cell Lines		
Phoenix-AMPHO	ATCC	Cat# CRL-3213, RRID:CVCL_H716
Human: Normal Human Dermal Fibroblasts (NHDFs)	Lonza	Cat# CC-2509
African green monkey: BSC-40	Dr. Ian Mohr (NYU-Lagone, New York, NY, USA)	N/A
African green monkey: Vero	Dr. Ian Mohr (NYU-Lagone, New York, NY, USA)	N/A
SK-N-SH	Dr. Patricia Spear (Northwestern University, Chicago, IL, USA)	N/A
Oligonucleotides		
Silencer® Negative Control #1 siRNA	Thermo Fisher Scientific	Cat# AM4635
EB1 siRNA	Thermo Fisher Scientific	siRNA ID: 3891
EB1 siRNA	Thermo Fisher Scientific	siRNA ID: 21079, 136575
EB3 siRNA	Thermo Fisher Scientific	siRNA ID: 19984
CLIP-170 siRNA	Thermo Fisher Scientific	siRNA ID: 142517
TACC3 siRNA	Thermo Fisher Scientific	siRNA ID: 135672, 3056
Kif5A siRNA	Thermo Fisher Scientific	siRNA ID: s7837
Kif5B siRNA	Thermo Fisher Scientific	siRNA ID: s731
Kif5C siRNA	Thermo Fisher Scientific	siRNA ID: s7842
Forward primer for untagged TACC3 amplification: GCAGCGGCCGCGCCACCATGAGTCTGCAGGTCTTAAAC	N/A	N/A
Reverse primer for untagged TACC3 amplification: GCAACCGGTTTAGATCTTCTCCATCTTGGA	N/A	N/A
Forward primer for FLAG-TACC3 amplification: GCAACCGGTGCCACCATGGACTACAAAGACGATGACGACAAGAGTCTGCAGGTCTTAAAC	N/A	N/A
Reverse primer for FLAG-TACC3 amplification: GCAGGATCCTTATCTAGAGATCTTCTC	N/A	N/A
Recombinant DNA		
pBABE-PURO-AA-GFP-CLIP-170	Dr. Derek Walsh (Northwestern University,	Procter et al., 2018

REAGENT or RESOURCE	SOURCE	IDENTIFIER
	Chicago, IL, USA)	
pBRAIN-GFP-TACC3-KDP-shTACC3	Addgene	Cat# 59356
pQCXIP-TACC3	this paper	N/A
pQCXIP-FLAG-TACC3	this paper	N/A
Software and Algorithms		
FIJI (ImageJ installation)	Open source	http://fiji.sc; RRID:SCR_002285
MetaMorph Microscopy Automation and Image Analysis Software	Molecular Devices	RRID:SCR_002368
GraphPad Prism (Version 7)	Graphpad	RRID:SCR_002798
Other		
Leibovitz's L-15 Medium, containing no phenol red	Thermo Fisher Scientific	Cat# 21083027
Cell view four compartment 35 mm glass-bottom dish	Greiner Bio-One	Cat# 627870